Strongly Anisotropic Thermomechanical Response to Shock Wave Loading in Oriented Samples of the Triclinic Molecular Crystal 1,3,5-Triamino-2,4,6-Trinitrobenzene (TATB)

Puhan Zhao,[‡] Matthew P. Kroonblawd,[†] Nithin Mathew,[¥] and Tommy Sewell[*,‡]

[‡] Department of Chemistry, University of Missouri-Columbia, Columbia, MO 65211

[†] Materials Science Division, Lawrence Livermore National Laboratory, Livermore, CA 94551

[¥] Theoretical Division, Los Alamos National Laboratory, Los Alamos, NM 87545

[*] sewellt@missouri.edu

ABSTRACT: All-atom molecular dynamics simulations were used to study shock wave loading in oriented single crystals of the highly anisotropic triclinic molecular crystal 1,3,5-triamino-2,4,6-trinitrobenzene (TATB). The crystal structure consists of planar hydrogen-bonded sheets of individually planar TATB molecules that stack into graphitic-like layers. Shocks were studied for seven systematically prepared crystal orientations with limiting cases that correspond to shock propagation exactly perpendicular and exactly parallel to the graphitic-like layers. The simulations were performed for initially defect-free crystals using a reverse-ballistic configuration that generates explicit, supported shocks. Final longitudinal stress components are between $\approx$8.5 GPa and $\approx$10.5 GPa for the 1.0 km s^{-1} impact speed studied. Orientation-dependent properties are reported including shock speeds, stresses, temperatures, compression ratios, and local material strain rates. Spatio-temporal maps of the temperature, stress tensor, material flow, and molecular orientations reveal complicated processes that arise for specific shock directions. The results indicate that TATB shock response is highly sensitive to crystal orientation, with significant qualitative differences for the time evolution of the stress tensor and temperature, elastic/inelastic compression response, defect formation and growth, critical von Mises stress, and strain rates during shock rise that span nearly an order of magnitude. A variety of inelastic deformation mechanisms are identified, ranging from crumpling of graphitic-like layers to dislocation-mediated plasticity to intense shear strain localization. To our knowledge, these are the first systematic MD simulations and analysis of explicit shock wave propagation along non-trivial crystal directions in a triclinic molecular crystal.

1. INTRODUCTION

Shock wave propagation in molecular crystals is complex owing to the typically low symmetry class, complicated molecular shapes and conformational flexibility, polymorphism and melting, and possible chemical transformations. Most previous molecular dynamics (MD) simulations of explicit shock waves in molecular crystals with symmetry class lower than tetragonal have been limited to propagation along 'trivial' directions such as $\mathbf{a'} = \mathbf{b} \times \mathbf{c}$ (and cyclic permutations among the lattice vectors $\mathbf{a}$, $\mathbf{b}$, and $\mathbf{c}$) that correspond to shocks propagating normal to (100), (010), or (001) crystal surfaces. By contrast, in many single-crystal shock experiments, the impact planes correspond to lower-index surfaces. Therefore, understanding the anisotropic single-crystal shock response along a generalized direction is critical for connecting atomistic simulations to experiments. It is also highly important for the reliable formulation and parameterization of continuum mesoscale models which increasingly are being used to simulate the single-crystal and grain-scale response of pressed powder aggregates and polymer composites.[1-18] The recently reported Generalized Crystal-Cutting Method (GCCM)[19] enables the construction, in principle, of two-dimensionally (2D) periodic cells suitable for MD simulations of shock wave propagation normal to any desired plane in crystals with arbitrary space group and asymmetric unit.

The molecule 1,3,5-triamino-2,4,6-trinitrobenzene (TATB) is an energetic compound that consists of a benzene ring with alternating amino ($-NH_2$) and nitro ($-NO_2$) groups bonded to it. Despite containing six pendent functional groups, the molecule is essentially planar due to the combined effects of push-pull electronic interactions[20] and intramolecular hydrogen bonding between adjacent H and O atoms around the ring, leading to D_{3h} point group symmetry. The crystal structure at standard ambient conditions is triclinic ($P\bar{1}$ space group) and consists of planar hydrogen-bonded sheets of individually planar TATB molecules that stack into graphitic-like

3

layers.[21] A monoclinic polymorph, also layered, has been reported recently at room temperature for pressures greater than 4 GPa.[22] The high degree of structural anisotropy leads to significant anisotropy in the mechanical,[23-34] thermal,[35-47] and spectroscopic[21] properties of the substance. See **Figure 1** for a view of a TATB crystal and additional information pertinent to the shock simulation geometry and crystal orientations studied here (detailed below). Given its anisotropic and triclinic structure and its practical role as the energetic constituent in certain plastic-bonded explosives (PBX) formulations such as PBX 9502 and LX-17,[48] TATB is attractive as a platform for studies designed to reveal the extent and implications of anisotropy on the thermomechanical response under a wide range of thermodynamic and loading conditions. It is particularly attractive from the view of atomic-scale methods development due to the triclinic symmetry. Equations and codes developed for triclinic crystals should be capable of handling all other crystal symmetry classes as special subcases.

Molecular dynamics simulations of explicit shock waves in TATB have been reported. The first of these was due to Fried and Tarver,[49] in a 1995 APS Shock Conference Proceedings article. These simulations were performed for 2D single sheets of TATB molecules with varying degrees of porosity (molecular vacancies in the sheets) based on the generic DREIDING[50] force field. Fried and Tarver reported that increasing porosity leads to decreased shock velocity, a broadened shock rise profile, increased shock temperature, and substantially increased shock relaxation times.

Long and Chen[51] reported MD simulations of shock-induced mechanics and chemistry in TATB, modeled using the Gee *et al.*[41] and ReaxFF[52,53] force fields, respectively. By combining the non-reactive and reactive results with the Hugoniot relations and the JWL[54] equation of state, Long and Chen were able to model the entire detonation wave profile of TATB from initial shock arrival to the onset of rapid chemistry; the Chapman-Jouget state (C-J, *i.e.*, sonic point in the wave

4

profile); and slow reactions, behind the C-J state, based on a simple kinetic model for carbon clustering. In a separate paper, using multiple force fields that were spliced together, Long and Chen[55] studied the effects of polycrystallinity and pore collapse on the thermo-mechanical response of crystalline aggregates of pure hexahydro-1,3,5-trinitro-1,3,5-triazine (RDX), RDX coated by TATB, and RDX coated by graphite.

A study of shock-induced pore collapse in TATB using both continuum and MD simulations was reported by Zhao *et al.*[15] A quasi-2D simulation cell containing a cylindrical pore in the MD simulations (for three different crystal orientations) and a 2D cell containing a circular pore in the continuum treatment were studied at three impact speeds chosen to span collapse mechanisms ranging from predominantly visco-plastic to hydrodynamic. The MD simulations used an all-atom non-reactive force field (the same one used here) and the continuum calculations were performed using a baseline isotropic, elastic-perfectly plastic strength model. Broad agreement for the shock dynamics, pore time-evolution profiles, and overall temperature distributions was obtained for the strongest shock, which yielded a predominantly hydrodynamic-like collapse mechanism. For the weaker shocks, differences between the MD- and continuum-based predictions, and strong sensitivity to crystal orientation in the case of MD, underscored the need for higher-fidelity continuum models under conditions for which material anisotropy and strength properties are important. The sensitivity of the continuum predictions to models for the melting curve ($T_{melt} = T_{melt}(P)$) and specific heat was also investigated.

A recent MD study of shock-induced chemical activation interior to nanoscale shear bands in single-crystal TATB was reported by Kroonblawd and Fried.[56] Using an all-atom non-reactive force field and a crystal orientation inspired by the present study—in particular the case $\theta = 75°$ discussed below, for which intense shear localization occurs—the authors extracted from the full

non-reactive simulation subsamples of material corresponding to regions of crystalline and sheared TATB behind the shock. The subsamples were subsequently studied using semiempirical density functional tight-binding (DFTB) 'quantum-MD' simulations. Kroonblawd and Fried showed that molecules in the shear bands are geometrically distorted and highly reactive compared to bulk crystal, and concluded that chemical activation *via* shear banding is a viable ignition mechanism under detonation conditions that may also support enhanced burn rates for weaker shocks. Shock collapse of pores leads to even larger molecular-level strains than seen in shear bands.[57] These strained states were shown to persist across typical hot-spot reaction time scales and are postulated to give rise to a mechanochemical acceleration of decomposition kinetics.

Many atomistic studies on TATB under shock conditions have focused on understanding its chemical reactivity, including cases with explicitly resolved shocks as well as shocks modeled using equilibrium methods (roughly akin to thermostats or barostats) such as the multiscale shock technique (MSST).[58] Two main advantages of equilibrium techniques are their applicability to small systems that can be resolved with quantum-based descriptions of the forces and the ability to reach very long time scales (>100 ps). The trade-off is that material dynamics in the shock rise are not necessarily captured accurately. Because the chemistry of TATB is exceptionally slow, inducing reactions within the time scale of a typical explicit-shock simulation requires both empirical potentials (*e.g.*, ReaxFF[52,53]) and massively overdriven shocks (*e.g.*, shock velocities u_s ~ 10 km s^{-1}).[59] Indeed, practically all chemistry-focused shock studies for TATB, whether simulated using explicit or equilibrium approaches, considered states that are well above the von Neumann spike pressure (~34 GPa[60]). An early MSST study using DFTB showed that strongly overdriven shocks (u_s = 9 km s^{-1}, shock pressure ~ 60 GPa) induce prompt decomposition within 100 ps followed by growth of nitrogen-containing heterocycles that retard further condensation to

solid carbon.[61] A more recent DFTB-based MSST simulation study with similarly strong shocks identified detailed inter- and intra-molecular decomposition mechanisms in the initially perfect crystal.[62] Sub-picosecond chemical reaction pathways were shown to vary with shock direction in DFT-based simulations using an omni-directional MSST, for the case of shocks with $u_s = 10$ km s^{-1}.[30] Augmentation of MSST with a colored thermostat can partially account for nuclear quantum effects missing in MD simulations.[63] This approach was applied to shock loading of TATB by Hamilton *et al.*[64] Those authors found that including a quantum specific heat and zero-point energy in the dynamics contributes to an increase in apparent reactivity for a given shock pressure.

Kroonblawd *et al.*[65] reported a study of TATB in which the all-atom non-reactive force field due to Bedrov *et al.*,[23] with modifications due to Kroonblawd and Sewell,[37] was used as the basis for parameterizing an energy-conserving all-atom, rigid-molecule dissipative particle dynamics (DPDE) model, which was then used to perform micron-scale simulations of shocks propagating normal to the (001) crystal surface. The DPDE model includes an adjustable parameter that governs the rate of energy exchange between the explicit external (molecular translational and librational) degrees of freedom and coarse-grain implicit (intramolecular) degrees of freedom,[66] the latter of which are modeled in a way that yields a quantum-like temperature-dependent specific heat *via* a two-oscillator Einsten model. The results showed significant sensitivity of the transient shock response to the adjustable parameter in the DPDE model, the likely implications of which were discussed in connection with mechanical dissipation behind the shock and the onset of chemistry.

Atomic-based studies of the non-shock mechanical response of TATB have also been reported. [22,24-26,28,29,67-69] Because of the nature of the crystal packing, plasticity involving slip between basal planes in TATB (the crystal exhibits two inequivalent basal planes) is expected to occur with much

lower barriers to dislocation glide (*i.e.*, stacking-fault energies),[70] in a fashion somewhat analogous to that in graphite,[71] compared to slip that occurs within a given molecular layer or that involves dislocation glide across multiple basal planes (both of which involve disrupting the intermolecular hydrogen-bonding network that exists within the layers). Indeed, using MD, very low stacking fault energies, and thus easy dislocation glide, were predicted for slip between adjacent basal planes both at zero kelvin[24] and at finite temperature.[25]

In a study that is particularly relevant to the present one, Lafourcade *et al.*[29] used all-atom but rigid-molecule MD in conjunction with the reaction field[72-74] approximation for electrostatic interactions to characterize plastic deformation mechanisms and energetics in crystalline TATB for a variety of different strain- and strain-rate loading paths. Of particular note is that Lafourcade *et al.* provided a molecular-based definition of the deformation-gradient tensor, which enables imposition of a generalized prescribed strain, and constant strain rate, in the simulations. Lafourcade *et al.* investigated several different loading paths, some of them similar to those studied here. They observed and characterized a variety of molecular-scale inelastic deformation mechanisms including basal-plane slip, a twinning/crumpling mechanism, and dislocations with Burgers vectors that involve 'breaking' of the hydrogen-bonded layers in the crystal. This study revealed a significant richness in the non-shock deformation behavior of TATB.

Here we present the results of MD simulations of shocks in oriented TATB single crystals. To our knowledge these are the first reported MD simulations of the explicit shock dynamics, for a triclinic molecular crystal, that systematically investigate the orientation sensitivity for non-trivial crystal orientations. We focus on relatively weak shocks ($\approx$8-10 GPa) propagating through initially defect-free crystals. The simulations were performed using a mechanically accurate but non-reactive force field. This is a reasonable approximation given the remarkably low shock-initiation

sensitivity of real TATB crystals,[48,75,76] which typically are rife with defects (cf. Figures 2 and 8 of Ref. 77), and the absence in the present simulations of introduced defect structures such as voids, dislocations, or grain boundaries that would serve as heterogeneous energy localization sites. In the following, we report orientation-dependent elastic and inelastic shock speeds, compression ratios, and local strain rates in the various shock rises; measures of local (kinetic) temperature, stress tensor, and von Mises stress; and the extent of loss, and in some cases recovery, of crystalline order in the wake of shock passage. We identify several different homogeneously nucleated deformation mechanisms ranging from crumpling to dislocation-mediated plasticity to intense shear-strain localization. It is not our goal to provide an exhaustive description of the nanoscopic deformation mechanisms that arise, but rather to survey the varieties of thermomechanical response in the crystal depending on the direction of shock wave propagation.

2. COMPUTATIONAL METHODS

2.1 Force Field. The simulations were performed using the LAMMPS code[78,79] in conjunction with the all-atom non-reactive TATB force field with fully flexible molecules originally due to Bedrov *et al.*[23] with subsequent refinements due to Kroonblawd and Sewell[37] and Mathew and Sewell.[40] This force field was shown to approximately reproduce measured pressure- and temperature-dependent lattice parameters,[21] experimental vibrational spectra,[37] and the heat of sublimation.[24] It has been used for predictions of the isothermal elastic tensor,[23,24] basal plane plasticity,[24,29] nanoindentation response,[26] thermal conductivity,[37-39] energy transport away from a hot spot,[80] the melt curve,[81] and liquid-state transport coefficients.[81] It was also used as the basis for parameterizing an energy-conserving DPDE force model that was subsequently applied to study shock compression of (001)-oriented TATB on approximately the micron spatial scale.[65]

LAMMPS input decks for the force field and a single unit cell of TATB are provided in the online supporting information.

2.2 Shock Geometry and System Construction. The simulations were performed using a reverse-ballistic configuration[82] wherein an oblong oriented crystalline slab of thermalized flexible molecules (the *sample*) strikes a rigid stationary slab composed of the same material (the *piston*). The sample and piston are structurally commensurate and the impact velocity vector $\mathbf{u}_p$ is directed normal to the piston-sample interface plane. The result is a shock wave that propagates through the sample with velocity vector $\mathbf{u}_w$ in the frame of the stationary piston. The shock is supported until it reaches the opposite end of the sample—the instant of maximum compression of the sample—after which a release wave propagates back through the sample. Due to material in-flow into the shock front in the reverse-ballistic configuration, the shock wave velocity in the commonly used shock frame[83] (in which the piston moves at constant speed into the initially stationary sample) is $\mathbf{u}_s = \mathbf{u}_w + |\mathbf{u}_p|$.

Simulation cells for seven different orientations, bracketed by limiting cases that correspond to shock propagation exactly perpendicular ($\theta \equiv 0°$) and exactly parallel ($\theta \equiv 90°$) to the surface-normal vector of the layers in the TATB crystal structure, were constructed using the GCCM[19] and TATB lattice vectors predicted by the force field at 300 K and atmospheric pressure. Five intermediate orientations were constructed that correspond to shock orientation angles $\theta = 15°$, $30°$, $45°$, $60°$, and $75°$. The angle θ is defined as that between the lattice vector **a** (which lies within the crystal layers) and the shock direction **S**. The shock direction is constrained to lie within the plane defined by lattice vector **a** and the basal plane normal vector $\mathbf{N}_{(001)} = \mathbf{a} \times \mathbf{b}$.

10

Generalized unit cells were built under the constraint that they will be approximately orthorhombic and have a simulation-cell-face normal vector aligned with **S**. These cells were replicated in three-dimensional (3D) space to yield primary simulation cells with edge lengths of approximately 100 nm parallel to **S** and approximately 10 nm for the cell edges transverse to **S**. The resulting systems contained between 78,192 and 105,792 molecules. The cells were rotated so that **S** was parallel to $+z$ in the Cartesian lab frame and a 5.0 nm gap was introduced along z at the 'top' of the samples to limit electrostatic interactions across the longitudinal periodic boundary during the shock simulations. **Figure 1** depicts the definition of θ with respect to the crystal lattice, a snapshot of a representative simulation cell prior to the beginning of the shock simulation, and zoomed-in views for all seven crystal orientations.

2.3 Numerical Details. Isochoric-isothermal (NVT) and isochoric-isoenergetic (NVE) trajectories were integrated using the velocity Verlet integrator[84] with a 0.25 fs and 0.10 fs time step, respectively. Systems were equilibrated at $T = 300$ K using a two-step process. First, a 5.0 ps NVE trajectory was integrated during which the atomic velocities were calculated every 10 fs and re-scaled to 300 K if $|T(t) - 300 \text{ K}| > 10$ K, with selection of new atomic velocities from the Maxwell distribution every 100 fs. This was followed by 100.0 ps of NVT integration using the Nosé-Hoover-style thermostat[85,86] in LAMMPS with the coupling parameter set to 100.0 fs.

Following equilibration, molecules with center-of-mass positions within 20 Å of the bottom of the primary cell ($z = 0$) at the beginning of the shock simulation were assigned to the piston, and their velocities were set to and then maintained at zero for the remainder of the simulation. The velocity vector $\mathbf{u}_p = (0, 0, -1.0 \text{ km s}^{-1})$ was added to the instantaneous thermal velocities of atoms in the flexible sample. Simulations for a given orientation were continued until the lead shock wave reached the free surface at the top of the sample (15.7 ps – 20.2 ps depending on the

orientation). The atomic positions, velocities, and stress tensor components were sampled every 100 fs during the shock simulations.

2.4 Analysis. Our focus is on the evolution of thermomechanical states behind the shock front(s) as functions of sample orientation, location in the sample, and time. We performed analyses of lead and secondary shock speeds, compression ratios behind the shock fronts, strain rates in the shock rises, local measures of kinetic temperatures (*i.e.*, kinetic energy densities scaled to temperature units, hereafter *temperatures*), stress tensor components, and molecular orientations. From the stress tensor we obtain the von Mises stress

$$\sigma_{\text{Mises}} = \left\{\frac{1}{2}\left[(\sigma_{11} - \sigma_{22})^2 + (\sigma_{22} - \sigma_{33})^2 + (\sigma_{33} - \sigma_{11})^2 + 6(\sigma_{12}^2 + \sigma_{23}^2 + \sigma_{31}^2)\right]\right\}^{1/2}, \quad (1)$$

which can be thought of as a maximum shear stress and therefore a driving force for plasticity and phase transformations. Here, the σ_{ij} are components of the stress tensor.

Spatiotemporal maps were computed by defining a framework of contiguous, platelike, 2D-periodic *fixed-volume bins* stacked along the shock direction **S**. At each instant of analysis, molecules were assigned to particular bins based on their center-of-mass z-coordinates. The instantaneous value of any property in a given bin was then calculated for that set of molecules. Spatial averages at a given instant were computed by using a moving average with a bin width of 10 Å and displacement increment of 3 Å. The shock front position at a given instant was defined as the mid-point along z of the bin with the largest gradient of the z-component of kinetic energy.[87,88]

Many of the property calculations have been described elsewhere.[87-89] In the following paragraphs, we comment briefly on the calculation of the stress tensor then describe how the compression ratios, strain rates, and molecular orientations were obtained.

The per-atom stress tensor was calculated using LAMMPS. The default algorithm used includes both kinetic and virial terms. Due to the kinetic term and the initial uniform impact velocity $\mathbf{u}_p = (0, 0, -1.0 \text{ km s}^{-1})$ of the sample, the local stress state for material ahead of the lead shock is not described accurately by this approach. However, this default definition *does* correctly capture the stress state behind the lead and subsequent shocks because of the reverse-ballistic configuration used; post-shock mass flow is the result of shock compression, which contributes to the stress state *via* the kinetic term. Stresses in a given fixed-volume bin were calculated by summing over the atomic stress tensors for all atoms in that bin at a given instant of analysis, with appropriate volume scaling. Note that we report stress components as $P_{ij} \equiv -\sigma_{ij}$. This was done simply so that the signs of the normal stresses in compressed material are positive. Note also that we do not report scalar pressures, as many of the final mechanical states were decidedly non-hydrostatic.

Compression ratios $\eta_i = L_i/L_0$ (i = 1 or 2) were calculated from individual system observations for material behind the lead shock (i = 1) and the second shock (i = 2, where applicable). Both compression ratios were determined relative to the unshocked sample. The approach used employs mass (*i.e.*, number of molecules) as the independent variable and length of sample containing that mass (*i.e.*, specific length) as the dependent one. The specific length that contains the prescribed definite mass is calculated for uncompressed material (L_0), material behind the lead shock (L_1), and behind the second shock where applicable (L_2). Assuming that both a lead shock and a second shock are present, the width of the plateau between them was subdivided into $N_{\text{sample,1}}$ contiguous sample regions, taking care to avoid the shock rises on either side of the plateau. The approximate number of molecules contained in the individual subregions was determined based on center-of-mass z-positions, and a nearby whole number N_{basis} was chosen to define the

mass basis for the remainder of the calculation. From this, the mean specific length along the sample between the shock rises was determined based on $N_{\text{sample,1}}$ samples, along with the standard deviation σ_1. This yields $L_1 \pm \sigma_1$. Using the same value for N_{basis}, numbers of samples $N_{\text{sample,0}}$ that would fill the unshocked sample, and $N_{\text{sample,2}}$ that would fill in the region between the second shock and the piston, were determined. From these, mean specific lengths and uncertainties $L_0 \pm \sigma_0$ and $L_2 \pm \sigma_2$ were determined, and thence, the compression ratios η_1 and η_2 and their uncertainties calculated. Typically, $N_{\text{basis}} \sim 1000$, $N_{\text{sample,0}} \sim 80$, $N_{\text{sample,1}} \sim 10$, and $N_{\text{sample,2}} \sim 40$; specific values for each orientation, along with a figure demonstrating the locations of sample regions ($N_{\text{sample,1}}$ and $N_{\text{sample,2}}$) for $\theta = 0°$, are provided in **Table S1** and **Figure S2**, respectively, of the online supporting information. An alternative, molecular-based approach for obtaining the compression ratios that yields equivalent results is also provided in the supporting information.

Strain rates during the shock rises were calculated using profiles of the longitudinal component of the particle velocity, v_z. This quantity was chosen because it captures material flow along the shock direction, is not kinetically limited, and was found to vary relatively smoothly along the length of the sample in comparison to other properties. Values of v_z just ahead of and just behind a given shock rise were extracted from the profiles and the positive difference Δv_z was defined as $\Delta v_z = v_{z,\text{ahead}} - v_{z,\text{behind}}$. The gradient term dv_z/dz along the length of the sample was obtained using a five-point central-difference scheme. This quantity is sharply peaked to negative values in the regions of shock rise and fluctuates about zero elsewhere, such that the width w_{rise} of a given shock rise can be obtained as the distance between first zeros on either side of the shock. From this, the strain rate $\dot{\varepsilon}$ for a given shock rise in a given system observation was defined as $\dot{\varepsilon} = \Delta v_z/w_{\text{rise}}$. Mean values and standard deviations of $\dot{\varepsilon}$ for each shock rise (*i.e.*, lead and, where applicable, second) were obtained from independent analyses performed for multiple system

observations as the shocks propagated through the sample. An illustration of Δv_z and w_{rise} for a single observation from the $\theta = 45°$ shock is provided in **Figure S4** in the online supporting information.

A simple molecular-based orientation parameter was calculated for the set of molecules in a given fixed-volume bin at a given instant. We defined this parameter as the angle φ formed by the TATB benzene-ring normal vector and the lab-frame basis vector $\hat{z}$, which is parallel to the shock direction **S** in all cases. At each instant of analysis, the mean value of the angle, $< \varphi >$, and the standard deviation were computed over all the molecules with center-of-mass z-position within a given fixed-volume bin. Values of φ for molecules in perfect, unshocked crystals are either equal or trivially related *via* the complement of the angle due to the centrosymmetric $P\bar{1}$ crystal structure, which leads to inversion symmetry between the two molecules in the primitive unit cell. For individual φ values greater than 90°, we used the complement.

Near-neighbor relative displacement maps (NNRDs) were used to characterize shock-induced molecular-scale displacements such as slip and amorphization. These were introduced by Zimmerman[90] and have been applied for the analysis of shocked α-HMX (octahydro-1,3,5,7-tetranitro-1,3,5,7-tetrazocine) by Jaramillo *et al.*[91] and PETN-I (pentaerythritol tetranitrate) by Eason and Sewell.[89] The NNRD is defined as the difference between relative Cartesian molecular center-of-mass position vectors for selected pairs of molecules behind the shocks and those same vectors for molecules in the perfect crystal. Based on the crystal structure, each TATB molecule has 14 near neighbors (six, arranged hexagonally, in the molecular layer containing the molecule; three apiece in the layers immediately above and immediately below the central molecule; and one apiece in the layers two above and two below the one containing the central molecule, which are symmetry equivalents to the central molecule); see **Figure 2**. This was determined based on the

15

unshocked, energy-minimized crystal and is independent of crystal orientation. For the perfect-crystal reference structures, it is necessary to account for the uniaxial compression that occurs behind a given shock in a given orientation. This was accomplished separately for each orientation behind the final shock rise (with known compression ratios η_1 or η_2 as applicable) by affinely scaling all of the atomic z-coordinates in the perfect, 3D-periodic unshocked crystal by η_i and then re-minimizing. (Although obviously this simple procedure distorts intramolecular geometries, we determined that these distortions relax within just a few minimization steps for the rather small η_i relevant to our study. We further verified that the procedure did not lead to structural rearrangements for any combination of crystal orientation and compression ratio studied.) Based on individual system observations made close to the time of maximum compression of the sample, NNRDs were calculated for each molecule, taking care to exclude molecules close to any shock rise, the piston, or the free surface.

3. RESULTS AND DISCUSSION

3.1. Overall Mechanical States. Supported shocks in TATB were simulated for seven different sample orientations. The longitudinal stress component P_{zz}, threshold von Mises stress, temperature, shock speed(s), compression ratio(s), and strain rate(s) as functions of sample orientation are summarized in **Figure 3**. The P_{zz} and temperature results (panel (a)) were evaluated at maximum compression as spatial averages over a region well behind the final shock, and also well in front of the piston, where those properties were approximately constant. The threshold von Mises stress for a given orientation was defined as the average of the 50 largest values of σ_{Mises} obtained for the fixed-volume bin centered at $z = 60$ nm. The speeds of the lead and (where applicable) second shocks are shown in panel (b). The first and second compression ratios (panel

(c)) and strain rates (panel (d)) were computed behind or in the lead and second shock rises, as applicable.

The P_{zz} values range between 8.5 and 10.5 GPa (**Figure 3**(a), blue, right-hand ordinate) and the orientation dependence is not monotonic. Values for $\theta = 75°$ and $90°$ exhibit relatively high uncertainty for reasons elaborated below (Secs. 3.2.4 and 3.2.5). The threshold von Mises stress shows significant anisotropy depending on the orientation, with values ≈ 3 GPa for $\theta < 45°$ and > 6 GPa for $\theta \geq 60°$.

Bulk shock heating is modest and varies approximately monotonically with respect to orientation angle (red, left-hand ordinate). The temperature jump is the least for $\theta = 0°$ and $15°$ cases ($\Delta T \approx 75$ K) and greatest when the shock propagates perpendicular to the crystal layers ($\theta = 90°$, $\Delta T \approx 113$ K). As was the case for P_{zz}, the shock temperatures for $\theta = 75°$ and $90°$ are also relatively imprecise. For the orientation $\theta = 75°$, there are three pronounced spikes in the analysis region that correspond to narrow subregions of intense local deformation (see Sec. 3.2.4 below and also Ref. 56, which was inspired by the present study). These localization events lead to narrow spikes in the T values in those subregions and the corresponding peak temperatures are shown as individual data points (open squares) in **Figure 3**(a). The temperatures in those subregions were excluded from the averaging used to obtain T for the $\theta = 75°$ case.

The shock-temperature jumps are lower than would be obtained in reality because the simulations are purely classical and therefore governed by the classical specific heat,[92] which is an upper bound to the quantum mechanical specific heat. For TATB the specific heat does not approach the classical limit until temperatures far in excess of those achieved in the present study (cf. Figure 1 of Ref. 65). Cawkwell *et al.*[93] used a simple Mie-Grüneisen equation of state analysis to estimate the classical error in the temperature jump in their MD study of shocks in (100)-oriented

α-RDX. The shock strength considered in that study was similar to those studied here and the dominant mode of stress relaxation was found to be shear-band formation. Using experimentally derived values for the isochoric specific heat, c_v, and Grüneisen coefficient, Γ, in conjunction with their simulated compression ratio, Cawkwell *et al.* concluded that the expected temperature increase due to the combined effects of isentropic compression and shock heating—but ignoring contributions due to viscous heating—is approximately four times larger than was obtained in their simulations for nascent shock-compressed crystal away from regions of shear localization. The factor of four was regarded as a lower limit as the thermodynamic analysis used constant values for c_v and Γ. There is no obvious reason to expect a qualitatively different conclusion for the present system.

The shock speeds are shown as functions of orientation in **Figure 3(b)**. For the lead shocks (red), the speeds range between 4.8 km s^{-1} and 6.0 km s^{-1}. There is a single minimum in the lead shock speed at $\theta = 45°$, maxima at the limiting angles 0° and 90°, and seemingly smooth variation over the entire orientation interval. The global maximum occurs at $\theta = 0°$. Well-defined second shocks were identified for $\theta \leq 30°$ and $\theta = 60°$, and only single waves were unambiguously identified for $\theta = 45°$ and 90°. For small θ, the second shock speed (≈ 5.7 km s^{-1}) is nearly independent of orientation angle, which is consistent with the intuitive expectation of extensive plastic deformation (crumpling) for shocks propagating parallel to the molecular layers. For larger θ, deformations are distinct depending on the crystal orientation. For $\theta = 60°$, a two-wave structure is apparent. For $\theta = 75°$, the second shock wave is ambiguous, as it is observed only for a short time at the beginning of the simulation before it interacts with the reflected wave from a mechanically distinct region of intense shear deformation that forms approximately 15 nm from the piston.

The compression ratios and local material strain rates are depicted in **Figures 3(c)** and **3(d)**, respectively. For $\theta \leq 30°$, the lead shock compression ratios η_1 are all small, between 0.95 and 1.0. For larger θ, η_1 is between 0.80 and 0.85. Interestingly, the overall volumetric compression is essentially independent of sample orientation for the 1.0 km s^{-1} impact strength studied here. The strain rates in the lead shock rises vary monotonically between 9×10^{10} s^{-1} for small θ and 7×10^{11} s^{-1} for $\theta = 90°$. Strain rates in the second shocks are only weakly dependent on sample orientation, with values close to 1×10^{11} s^{-1}. These strain-rate values are typical of what is observed in explicit MD shock simulations.[94,95] Probable fundamental explanations include the very steep loading profile and absence of pre-existing defects in the simulations. Experimental loading profiles will typically be much wider and inevitable pre-existing defects in real samples act as energy scattering sources that tend to lead to dispersion of the shock fronts. Additionally, the strain rates we calculate are almost certainly below experimental time resolution. We note that Crowhurst *et al.*[96] reported strain rates similar to the ones reported here in ultrafast shock excitation experiments on Al samples shocked to very high pressures, but to our knowledge such large experimental strain rates have not been reported for molecular systems.

3.2. Mechanical Response in Space and Time. In this subsection we present more detailed results for several additional properties for the cases $\theta = 0°$, 45°, 60°, 75°, and 90°, in **Figures 4-8**, respectively. For all five figures, in panels (a)-(c) we use time-position diagrams (*t-z diagrams*) to depict, as simultaneous functions of time and location in the samples, the intermolecular temperature T_{inter} (panel (a)), longitudinal stress component P_{zz} (panel (b)), and von Mises stress σ_{Mises} (panel (c)). Panels (d)-(f) depict, respectively, the local particle-velocity vector, the six stress tensor components (P_{xx}, P_{yy}, P_{zz}, P_{xy}, P_{xz}, and P_{yz}), and average molecular orientation $< \varphi >$ as functions of distance along the shock direction at chosen instants of time indicated by white

dashed horizontal lines in panels (b). The results for $\theta = 0°$, 15°, and 30° in this subsection are

qualitatively similar, thus only $\theta = 0°$ is discussed in detail; analogous figures for $\theta = 15°$ and 30°

are provided in the online supporting information.

3.2.1. $\theta = 0°$. For $\theta = 0°$ (**Figure 4**), in which case the shock propagates exactly parallel to

the molecular layers (see **Figure 1**), a two-wave structure is clearly apparent in the t-z diagrams

for T_{inter}, P_{zz}, σ_{Mises}, and particle velocity component v_z; and weakly apparent in P_{xx}, P_{yy}, v_x, v_y,

and the spatial profile for $< \varphi >$. Following a sharp transient, a steady-fluctuating intermolecular

temperature behind the second shock is established within ≈ 3 ps that is fairly uniform across the

length of the sample for a given time since shock passage (panel (a)). The peak T_{inter} values, ≈ 800

K, are large but well below the melting point that would exist for the range of 'pressures' studied

here.[81] Also, critically, T_{inter} is a measure of kinetic energy among only three out of 72 degrees of

freedom per molecule, namely those for local relative translations of molecular centers of mass.

The remaining degrees of freedom do not achieve similarly large kinetic energies during the shock.

The probability of chemistry is very small.

Mass flow behind the shocks is negligible, as evidenced by the transverse particle velocity

components v_x and v_y (panel (d)). The results for $\theta = 15°$ and 30° (not shown) exhibit larger, but

still small, extents of structured and correlated local transverse mass flow behind the shocks. This

is unsurprising as the basal crystal planes, between which dislocation slip is presumably least

hindered, align more closely with the direction of maximum resolved stress as $|\theta - 45°|$ tends to

zero. The spatial profile of the average orientation angle $< \varphi >$ is shown in panel (f), where the

uncertainties reflect one standard deviation accumulated over the molecules in a given fixed-

volume bin at the instant of analysis. Ahead of the lead shock, the values oscillate with small

variance about $< \varphi > \approx 87°$. Lead shock passage only causes a small decrease in $< \varphi >$ and a

20

small increase in the standard deviation. As the second shock passes, $< \varphi >$ decreases sharply by $\approx 20°$ and the uncertainty increases by approximately a factor of five. In the ≈ 40 nm between the second shock front and the piston, the value of $< \varphi >$ gradually increases (by $\approx 10°$) while the standard deviation remains practically constant.

$\underline{3.2.2. \; \theta = 45°.}$ For the case $\theta = 45°$ (**Figure 5**), the shock direction is at 45° relative to the crystal layers. In this case, a single wave, which we interpret as an overdriven plastic wave, is observed. As with the $\theta = 0°$ case, T_{inter} rises sharply at the shock front (panel (a)). In this case, however, the evolution toward a steady-fluctuating state occurs more slowly over several ps and the state behind the shock is relatively inhomogeneous at a given post-shock time. The values of P_{zz} and P_{xx} are almost identical over the entire simulation whereas P_{yy} is only about 50% as large and exhibits a subtle relaxation well behind the shock front (panel (e)).

The dominant feature in the particle velocity profile (panel (d)) is abrupt accelerations of v_x to non-zero values, which persist for a significant distance behind the shock. The ultimate approach of v_x back to zero coincides with the slight relaxation in P_{yy} noted just above. Also correlated with these relaxations, albeit with a slight time lag, is a substantial decrease in the width of the distribution of the orientation angle φ to essentially pre-shock values (panel (f)). Overall, $< \varphi >$ decreases by less than 5° immediately behind the shock but with substantial broadening of the distribution, and then again by a similar amount some 35 nm behind the shock front. Collectively, the results for $\theta = 45°$ suggest a structural transformation from an ordered state ahead of the shock to one characterized by extensive molecular disorientations close behind the shock, followed by a subsequent re-organization. What is perhaps most interesting is that final structure has a different orientation than the starting material, at least in the lab frame.

3.2.3. $\theta = 60°$.

For $\theta = 60°$, a two-wave structure is obtained (**Figure 6**). In contrast to the $\theta = 0°$ case, here most of the shock heating is associated with the lead shock (panel (a)). The longitudinal particle velocity component v_z changes almost immediately from $-|\mathbf{u}_p|$ to ~20 m s^{-1} behind the lead shock, with subsequent slow relaxation further toward zero (panel (d)). At the same time, components v_x and v_y abruptly achieve nearly constant, non-zero values. When the second wave passes, all three particle velocity components become zero. Based on the von Mises stress (panel (c)), the orientation angle (panel (f)), and the stress tensor components (panel (e)), the system remains crystalline over the entire simulation. Note especially from panel (f) that the mean value of φ decreases only by a few degrees with arrival of the lead shock, after which $< \varphi >$ is essentially constant. The only evidence of the second shock in panel (f) is a subtle, transient increase in the standard deviation that occurs just *behind* the second shock. Preliminary analysis of displacements of near-neighbor molecules suggests that the inelastic deformation in this case is characterized by a shear in the **a** direction about the basal plane.

3.2.4. $\theta = 75°$.

The responses for $\theta = 75°$ and $90°$ (**Figures 7** and **8**, respectively) are more complicated than for other angles. For $\theta = 75°$, we conclude that there is essentially a single, overdriven shock for which localized defects nucleate in (or immediately behind) the shock front, then grow, at regular spatial intervals. The t-z plots for T_{inter} (panel (a)) and the von Mises stress σ_{Mises} (panel (c)) suggest the beginnings of a two-wave structure for distances within 15 nm of the piston. In both panels one can see a faint second wave that propagates from the piston more slowly (*i.e.*, with higher slope in the figures) than the lead shock. Clearly evident in T_{inter} is the nucleation of hot spots in the lead shock rise. These occur at approximately 15 nm intervals as the shock propagates through the sample. In each instance, they form, then begin to decay, then reconstitute and persist for at least 5-10 ps. The second wave mentioned above reflects from first of these

defects as can clearly be seen in both T_{inter} and σ_{Mises}. Indeed, for the latter, ringing between the piston and the first defect is clearly visible. Whereas the transverse stress components P_{xx} and P_{yy} oscillate widely behind the shock, in correlated fashion and with spikes that correspond to the hot spot locations (panel (e)), P_{zz} rises sharply almost to the longtime value, which is approached gradually over the remainder of the simulation (panels (b) and (e)). Analogous comments apply to the particle velocities (panel (d)). The shock leads to very little displacement either in magnitude or standard deviation of the orientation angle φ (panel (f)). However, in the 'defect zones' $<\varphi>$ jumps back essentially to the value for unshocked material and the standard deviation of φ in those regions increases by factors of three or more. The small change in φ is consistent with the sample orientation, for which the shock direction is nearly perpendicular to the crystal stacking planes (see **Figure 1**).

A more detailed analysis of the shock response for the $\theta = 75°$ orientation, including a discussion of potential implications for hot-spot formation and ignition, is available in Ref. 56. In that study, which was performed for larger systems and considerably stronger shocks than studied here (impact speed $u_p = 2.5$ km s^{-1} *vs.* 1.0 km s^{-1}), Kroonblawd and Fried observed that, in addition to intense shear localization predominantly parallel to the molecular layers as shown in the present study, a network of shear bands also formed at angles of approximately 45° with respect to the shock direction. Interestingly, temperatures in the shear bands parallel to the molecular layers were found to be higher than those at 45°.

3.2.5. $\theta = 90°$. For $\theta = 90°$ (**Figure 8**), the shock direction **S** is exactly perpendicular to the plane of the molecular layers in the crystal (see **Figure 1**). Intuitively, from a continuum mechanics perspective, among the seven crystal orientations studied here this is the one for which the driving force for defect nucleation is the least: the shock wave is incident on stacked, planar sheets of

approximately planar molecules. The resolved shear stress on basal-plane slip systems is a minimum, and the longitudinal stress would not obviously drive the formation of crumpling of layers oriented parallel to it as was the case for $\theta = 0°$. However, the MD results suggest a much richer behavior when the relevant scales approach molecular dimensions. Based on P_{zz} (panel (b)), the particle velocities (panel (d)), and the orientation angle profile at distances close behind the shock (panel (f)), there would appear to be a simple, single shock wave. Moreover, as the shock wave propagates through the sample, at early post-shock times T_{inter} (panel (a)) exhibits the characteristic narrow transient followed by overall relaxation that, in this case, occurs on approximately a 5 ps time scale (panel (a)). However, across the entire length of the sample, the t-z diagram for T_{inter} in that early post-shock time interval exhibits considerable heterogeneity including numerous locations for which T_{inter} is almost as large as in the temperature spike associated with the shock rise. The molecules are translationally strongly perturbed. Approximately 10 ps behind the shock, hot spots, clearly associated with excursions in the intermolecular temperature field and nucleated immediately behind the shock, begin to grow into the sample. In contrast to the other shock orientations studied, the propagation of hot spots into nearby material with slow, well-defined speeds ($\pm \, dz/dt$) clearly suggests activation of a deformation mechanism that spans multiple hydrogen-bonded layers in the crystal.

Individual TATB molecules are essentially highly oblate ellipsoids. Under shock compression perpendicular to (001), sheets of molecules are squeezed together. The nascent stress state behind the shock front has $P_{zz} \gg (P_{xx} \approx P_{yy})$. Even under shock compression, the in-plane compression elastic coefficients C_{11} and C_{22} are much larger than the out-of-plane coefficient C_{33}; and likewise for the pure shear coefficients for which $C_{66} \gg (C_{44} \approx C_{55})$.[23,24] These factors combine to create an unstable equilibrium such that, if a local fluctuation (*e.g.*, a sufficiently large molecular

disorientation) occurs, the in-plane compression will tend to drive that disorientation further out of the plane, whether simply orientationally or possibly translationally also. This perturbs the molecules in adjacent layers, and the result is defect growth that cuts across the molecular layers.

The $\theta = 90°$ shock geometry was studied by Kroonblawd *et al.*[65] using a DPDE model in which individual molecules, though described with all-atom resolution, were treated as rigid bodies with only center-of-mass rotations and translations as *explicit degrees of freedom*. The heat capacity for internal molecular degrees of freedom—*implicit degrees of freedom*—was treated quantum mechanically using a mesoparticle description introduced by Strachan and Holian.[66] The strength of coupling between the implicit and explicit degrees of freedom is an adjustable parameter in the Strachan-Holian approach, and Kroonblawd *et al.* studied the sensitivity of energy-relaxation time scales to that parameter under non-shock conditions in some detail. Using the 'best' coupling parameter value, shocks propagating parallel to $\mathbf{N}_{(001)}$ were simulated using the same reverse-ballistic configuration employed here, for impact speeds of 1.0 km s^{-1}, 2.0 km s^{-1}, and 3.0 km s^{-1} in samples of approximately one-micron length parallel to the shock direction. Interestingly, Kroonblawd *et al.* reported the formation of defects highly reminiscent of those observed here for the same shock orientation (cf. Figure 8 of Ref. 65). They discussed the sensitivity to the implicit-explicit coupling strength and the effects of that on the time evolution of quiescent shock states behind the shock front. The present results for $\theta = 90°$ are broadly consistent with those of Kroonblawd *et al.*

3.3. More Detailed Analysis. In this subsection we present the radial distribution functions for all seven orientations (**Figure 9**), calculated separately for initially in-plane and out-of-plane molecular pairs; molecular-scale time sequences of representative deformations for $\theta = 0°$, 45°, 75°, and 90° (**Figure 10**); a more extensive sampling of deformations for $\theta = 90°$ (**Figure 11**);

and system-scale depictions of the deformation that has formed by the instant of maximum compression of the samples for all seven orientations (**Figure 12**). These provide more detailed molecular-scale insights as to how shock-induced plasticity differs from one orientation to the next. As will be shown below in Secs. 3.3.2 and 3.3.3, several distinct types of unit deformation behaviors were detected: basal plane slip between adjacent graphitic layers, crumpling within the graphitic layers, non-basal slip that breaks the graphitic layers, and extensive shear localization.

3.3.1. NNRD radial distribution functions. **Figure 9** contains radial distribution functions of the NNRDs, calculated for initially in-plane and out-of-plane molecular pairs (panels (a) and (b), respectively). The peaks in the radial distribution functions indicate the range and intensity of local deformations for each orientation and help to locate and categorize the deformation mechanisms (larger distances are shown, on a logarithmic scale, in the panel insets). Most of the deformations have displacement distances less than 5 Å. For $\theta = 75°$ and $90°$ cases, displacement distances extend to more than 20 Å, which correspond to dislocation slip of several molecular layers (demonstrated in **Figure 10**).

3.3.2. Depictions of local deformation mechanisms. **Figure 10** contains sequences of snapshots of small sub-regions in the samples prior to shock arrival (left), during shock traversal across the subregion (center), and after the shock has passed (right). From top to bottom, the crystal orientations are $\theta = 0°$, $45°$, $75°$, and $90°$, respectively. In all cases, the shock propagates vertically upward. The sub-regions shown were defined first by identifying a molecule in the sample that exhibits large NNRD values with respect to one or more of its 14 near neighbors (refer to **Figure 2**). We term this set of 15 molecules, excised from the larger sample for visualization purposes, a first-generation cluster. A second-generation cluster is obtained by identifying and adding the non-redundant near neighbors of the first-generation cluster molecules; a third-

generation cluster by identifying and adding the non-redundant near neighbors of the second-generation cluster molecules; and so on. The results shown in **Figure 10** correspond to a fifth-generation cluster (which always contains 671 molecules). The color scheme used was chosen as a guide for the eye and is generally consistent with what is shown in **Figure 2**. In the $\theta = 0°$ case (top row), for which the shock propagation direction is parallel to the molecular layers, crumpling deformations are clearly apparent. For $\theta = 45°$ (second row), for which the shock direction is at $45°$ relative to the molecular layers, there is little to no basal plane slip. (This is somewhat surprising since for this orientation the resolved shear stress on the basal planes is nominally maximized. Albeit, the compression resulting from the shock would also result in a higher barrier for basal slip.) Rather, a structure reminiscent of the crumpling in the $\theta = 0°$ case forms that presumably significantly hinders slip. For the case $\theta = 75°$ (third row), extensive shear localization occurs through slip in basal and non-basal planes. Although the magnitudes of both local shear strain and molecular orientational disorder are comparatively large, the shear strains evolve initially *via* a sequence of partial and full dislocations that nucleate and glide. Note that although the material undergoes extensive shear deformation, the molecular packing is locally relatively well-preserved, albeit with large rearrangements of instantaneous molecular near-neighbors, presumably due to the strongly oblate-ellipsoidal shape of the molecules. For the case $\theta = 90°$ (bottom row), the deformation shown corresponds to a non-basal dislocation. In the center image, a stacking fault is evident, whereas at longer time (right-hand image) the presence of a clear dislocation is readily evident. (Due to the existence of two inequivalent basal planes in the crystal (dubbed *P1* and *P2*, which are parallel and stack in a …*P1, P2, P1, P2*… arrangement), dislocation slip by a single molecule layer comprises a stacking fault; a full dislocation requires slip by two molecular layers.) The slip resulting from this dislocation was found to be dominantly in the **a** and

c directions (*i.e.*, a slip vector of the [-101] type), with a smaller but non-negligible displacement in **b**.

Although the deformation mechanism depicted in **Figure 10** for $\theta = 90°$ is clearly resolved dislocation slip in non-basal planes, the situation for that crystal orientation is considerably more complicated than the figure suggests. To illustrate this, **Figure 11** contains additional sequences of deformation event for the $\theta = 90°$ crystal orientation. Panel (a) shows the simulation cell at the instant of maximum compression, colored by NNRD value and only depicting molecules with NNRD values above a threshold level. Panel (b) contains zoom-in views of the system for four small regions in the sample, at locations indicated in panel (a). Each column in panel (b) corresponds to a different region and the four rows in a given column correspond to different instants of time (all subsequent to initial shock passage). All four sequences end at the instant of maximum compression, $t = 18.0$ ps. For visual clarity, only the TATB benzene rings are shown. The projection direction varies from one column to the next so as to most clearly capture the behavior.

The results in **Figure 11** exhibit several interesting features. *For region I*, localization nucleation occurs in a pair of basal planes and involves molecular displacements both within and between the basal planes. The defect grows at an angle of approximately |45°| relative to the shock direction. Early in this stage the deformation is relatively broad and delocalized. However, by the time of maximum compression it has narrowed and intensified into a region of intense shear. *In region II* the deformation is mainly restricted to four contiguous basal planes, with notable retention of the overall planar structure. In both regions I and II, rotations of the local crystal structure are apparent in the vicinity of the defects. *Localization in region III* nucleates by dislocation slip, as can be seen by examining the relative displacements of the four circled

molecules in the sequence. Arrows indicate the slip direction, projected into the plane of the image sequence. The sample region contains a sliding defect[37] consisting of four basal planes. This defect disrupts the dislocation glide, leading to non-crystallographic breakdown of the local crystal structure that likely leads to the formation of a shear band; *likely*, as it is not fully formed by the end of the sequence. *Region IV* corresponds to the result shown for $\theta = 90°$ in **Figure 10**, where clean layer-breaking (non-basal) dislocation slip was apparent. Defect nucleation in this region occurs *via* dislocation slip, as denoted by the set of circled molecules and projected slip-direction arrows. Compared to region III where the crystallographic slip becomes disrupted, in region IV the deformation remains relatively ordered, although some degree of molecular translational and librational disorder is apparent both at the slip plane and close to it, as are small rotations of the local crystal structure.

The results shown in this subsection are merely examples of the dominant kinds of deformation that we observe locally for the various orientations studied. However, the deformations on larger scales are quite complex, as we demonstrate in the following subsection.

3.3.3. <u>Depictions of deformations in the entire simulation cell.</u> **Figure 12** contains full-system snapshots, extracted at the instants of maximum sample compression, for all seven orientations. Molecules near the pistons or the free surfaces were excluded from the analysis. In this rendering, individual molecules are colored according to the value of the largest NNRD among the 14 near neighbors. Also, to focus on regions where significant changes have occurred, molecules for which the maximum NNRD is less than some threshold value are not shown. Animations of the time evolution for all orientations are provided in the online supporting information. For $\theta \leq 30°$, crumpling is the dominant deformation mechanism, with a trend toward less-disordered crumpling from $\theta = 0°$ to $\theta = 30°$. The staggered twinning structure in the $\theta = 30°$ case is reminiscent of

the propagation of deformation in the 45° case. The 60° case is distinct from other orientations due to the absence of widespread deformation (the exclusion threshold is the lowest among all orientations; see **Table S2** of the online supporting information). The lead shock results in a concerted rotation of the basal planes by approximately 5° in the lab frame. This is followed by small (few unit-cell scale) localized regions of structural disruption with preservation of overall crystallinity. By contrast, both the $\theta = 75°$ and 90° cases exhibit significant shear deformations and dislocation glide. Note the shear deformations occur at almost equal intervals along z throughout the sample for $\theta = 75°$, but not for $\theta = 90°$. The deformation for the 90° case is initially due to stacking faults, followed by a full dislocation, which propagate parallel to both the $\pm z$-directions.

Similar, and in some cases almost identical, deformation mechanisms including crumpling, basal-plane gliding, and stacking-fault/full dislocation nucleation in non-basal plane were predicted in the isothermal non-shock MD study due to Lafourcade *et al.*[29] In that work, deformation mechanisms of TATB were investigated using a prescribed velocity gradient tensor that imposes a biaxial deformation. The authors focused on pure shear and uniaxial compression as special cases. Note that the prescribed strain rates (10^7-10^{10} s^{-1}) and the maximum compression (10%) in their simulations are both lower than results presented here. Nevertheless, similar deformation mechanisms are observed. The inelastic deformation mechanism was found to be strongly dependent on the orientation of the loading direction with respect to $\mathbf{N}_{(001)} = \mathbf{a} \times \mathbf{b}$; this agrees with the strong orientation dependence for shock loading observed in this study. At orientations such that the prescribed deformation had significant compression parallel to the molecular layers, crumpling deformation was predicted, similar to the deformation predicted in this work for $\theta < 45°$. Homogeneous nucleation of non-basal dislocations, shown above for $\theta =$

30

90° (see **Figures 10** and **11**), was also predicted by Lafourcade *et al.* for pure shear loading in certain cases. Notably in their study, both the crumpling and nucleation of non-basal dislocations were predicted to occur at similar threshold von Mises stress. However, in our simulations, the von Mises stress was found to increase to ≈ 3 GPa for cases where crumpling deformation was predicted ($\theta < 45°$) and > 6 GPa when non-basal dislocation slip was observed. This anisotropy in the threshold von Mises stress suggests a strong rate-dependence of the inelastic deformation mechanisms.

The comparison between the present explicit-shock results and the non-shock (but high strain rate) results of Lafourcade *et al.*[29] for $\theta = 90°$ is particularly interesting. In both cases there is strong evidence for non-basal dislocation slip. However, whereas Lafourcade *et al.* found that this is the dominant mechanism our simulations suggest that in many cases dislocation glide is disrupted, leading to the formation of shear bands. There are several possible, and interrelated, explanations for the difference.

Both Lafourcade *et al.*'s simulations and those reported here are based on all-atom representations of the molecular structure and using (essentially) the same underlying empirical force field. However, the present simulations used flexible molecules whereas Lafourcade *et al.* treated individual TATB molecules as rigid. Shock passage increases both the stress and temperature behind the shock and this affects the amplitudes of both molecular vibrations (absent in rigid-molecule simulations) and local molecular translations and librations in the crystal lattice. Shock passage also results in transient disequilibrium between the intramolecular and intermolecular degrees of freedom, with the latter being initially 'hotter' and the approach to local thermal equilibrium requiring several picoseconds.[87,88,97-99] This effect will not exist for rigid molecules. Another consideration is the existence of inequivalent basal planes of types *P1* and *P2*

in TATB crystal, and in particular the …*P1, P2, P1, P2*… basal plane stacking motif. Thus, a full layer-breaking dislocation requires slip by two molecular layers; slip by only one layer corresponds to an unstable stacking fault geometry (cf. **Figure 10** and Ref. 29), the formation of which requires local dilatancy of the crystal lattice (or perturbations to molecular geometry in the case of flexible molecules) to accommodate the structural mismatch between the two basal plane types. Finally, compression behind the shock significantly increases barriers to homogeneous dislocation nucleation and glide.[24,25]

These factors, combined with dynamic structural imperfections—whether relatively long lived (*e.g.*, sliding defects) or induced transiently behind the shock—all tend to hinder or disrupt smooth dislocation glide. Several of these factors are present in flexible molecules but not rigid ones, or are likely behind explicit shock waves but not (or less so) for homogeneous, isothermal deformations. Based on the present simulations, we tentatively conclude that layer-breaking dislocation slip may be a prominent localization *nucleation* mechanism for $\theta = 90°$, consistent with the results of Lafourcade *et al.*, but that extended glide of such dislocation will not be widespread, with most such nucleation events eventually transforming into shear bands, an effect that would be enhanced at shock pressures stronger than those studied here.[56,82,91]

4. CONCLUSIONS

Anisotropy in the shock wave response of the triclinic crystal 1,3,5-triamino-2,4,6-trinitrobenzene (TATB) was studied using molecular dynamics (MD) simulations. Shock propagation along seven chosen directions in the crystal was simulated. To our knowledge, these are the first MD simulations of explicit shock propagation in a triclinic crystal for systematically varied orientations other than those for which the shock propagation direction is parallel to cross products of the

fundamental unit-cell lattice vectors (*e.g.*, $\hat{\mathbf{c}}' = \hat{\mathbf{a}} \times \hat{\mathbf{b}}$ and cyclic permutations). The main observations are:

- For the same 1.0 km s^{-1} impact speed in all cases, some crystal orientations yield a distinct two-wave response, and others a single wave.

- Propagation speeds of the lead shocks differ by ~20 % depending on crystal orientation. Speeds of secondary shocks, where distinct from the lead shock, are relatively independent of crystal orientation.

- Local material strain rates in the lead shock vary by approximately an order of magnitude depending on crystal orientation. Strain rates in secondary shocks are toward the lower end of the range for the lead shocks and are relatively insensitive to crystal orientation.

- Post-shock relaxation of intermolecular temperature, stress state, and molecular orientations are highly sensitive to crystal orientation. The threshold von Mises stress varies approximately by a factor of two depending on the the crystal orientation.

- Deformation mechanism and growth are extremely sensitive to crystal orientations. Several inelastic deformation mechanisms are identified, ranging from crumpling to dislocation-mediated slip to intense shear localization.

ONLINE SUPPORTING INFORMATION

Illustration of a TATB single molecule; a LAMMPS example input script; coefficients for the repulsive pair interaction between oxygen and hydrogen; a Cartesian description for one unit cell of TATB; elaboration of the compression-ratio calculation used in the article, including an example and a table of orientation-specific parameter values used; an alternative approach for computing the compression ratio; elaboration of the strain-rate calculation, including an example;

spatio-temporal mechanical response for the $\theta = 15°$ and $30°$ cases; animations of the simulations; and a table of orientation-dependent NNRD threshold values.

ACKNOWLEDGMENTS

REFERENCES

[1] Austin, R. A.; Barton, N. R.; Reaugh, J. E.; Fried, L. E. Direct Numerical Simulation of Shear Localization and Decomposition Reactions in Shock-Loaded HMX Crystal. *J. Appl. Phys.* **2015**, *117*, 185902(1-15).

[2] Zaug, J. M.; Austin, A. R.; Armstrong, M. R.; Crowhurst, J. C.; Goldman, N.; Ferranti, L.; Saw, C. K.; Swan, R. A.; Gross, R.; Fried, L. E. Ultrafast Dynamic Response of Single-Crystal β-HMX (Octahydro-1,3,5,7-Tetranitro-1,3,5,7-Tetrazocine). *J. Appl. Phys.* **2018**, *123*, 205902(1-12).

[3] Rai, N. K.; Udaykumar, H. S. Void Collapse Generated Meso-Scale Energy Localization in Shocked Energetic Materials: Non-Dimensional Parameters, Regimes, and Criticality of Hotspots. *Phys. Fluids*. **2018**, *31*, 016103(1-22).

[4] Rai, N. K.; Udaykumar, H. S. Three-Dimensional Simulation of Void Collapse in Energetic Materials. *Phys. Rev. Fluids.* **2018**, *3*, 033201(1-25).

[5] Grilli, N.; Koslowski, M. The Effect of Crystal Orientation on Shock Loading of Single Crystal Energetic Materials. *Comput. Phys. Commun.* **2018**, *155*, 235-245.

[6] Grilli, N.; Duarte, C. A.; Koslowski, M. Dynamic Fracture and Hot-Spot Modeling in Energetic Composites. *J. Appl. Phys.* **2018**, *123*, 065101(1-12).

[7] Kim, S.; Wei, Y.; Horie, Y.; Zhou, M. Prediction of Shock Initiation Thresholds and Ignition Probability of Polymer-Bonded Explosives Using Mesoscale Simulations. *J. Mech. Phys. Solids.* **2018**, *114*, 97-116.

[8] Keyhani, A.; Kim, S.; Horie, Y.; Zhou, M. Energy Dissipation in Polymer-Bonded Explosives with Various Levels of Constituent Plasticity and Internal Friction. *Comput. Mater. Sci.* **2019**, *159*, 136-149.

[9] Luscher, D. l.; Addressio, F. L.; Cawkwell, M. J.; Ramos, K. J. A Dislocation Density-Based Continuum Model of the Anisotropic Shock Response of Single Crystal α-Cyclotrimethylenetrinitramine. *J. Mech. Phys. Solids*. **2017**, *98*, 63-86.

[10] Cawkwell, M. J.; Montgometry, D. S.; Ramos, K. J.; Bolme, C. A. Free Energy Based Equation of State for Pentaerythritol Tetranitrate. *J. Phys. Chem. A* **2017**, *121*, 238-243.

[11] Kittel, D. E.; Yarrington, C. D. A Physically-Based Mie-Grüneisen Equation of State to Determine Hot Spot Temperature Distribution. *Combust. Theor. Model*. **2016**, *20*, 941-957.

[12] Wood, M. A.; Kittell, D. E.; Yarrington, C. D.; Thompson, A. P. Multiscale Modeling of Shock Wave Localization in Porous Energetic Material. *Phys. Rev. B*. **2018**, *97*, 014109(1-9).

[13] Sakano, M. N.; Hamed, A.; Kober, E. M.; Grilli, N.; Hamilton, B. W.; Islam, M. M.; Koslowski, M.; Strachan, A. Unsupervised Learning-Based Multiscale Model of Thermochemistry in 1,3,5-Trinitro-1,3,5-triazinane (RDX). *J. Phys. Chem. A*. **2020**, *124*, 9141-9155.

[14] Nelms, M. D.; Kroonblawd, M. P.; Austin, R. A. Pore Collapse in Single-Crystal TATB under Shock Compression. *AIP Conf. Proc*. **2020**, *2272*, 050001(1-6).

[15] Zhao, P.; Lee, S.; Sewell, T.; Udaykumar, H. S. Tandem Molecular Dynamics and Continuum Studies of Shock-Induced Pore Collapse in TATB. *Propellants, Explos., Pyrotech.* **2020**, *45*, 196-222.

[16] Duarte, C. A.; Li, C.; Hamilton, B. W.; Strachan, A.; Koslowski, M. Continuum and Molecular Dynamics Simulations of Pore Collapse in Shocked *β*-Tetramethylene Tetranitramine (*β*-HMX) Single Crystals. *J. Appl. Phys*. **2021**, *129*, 015904(1-15).

[17] Kroonblawd, M. P.; Austin, R. A. Sensitivity of Pore Collapse Heating to the Melting Temperature and Shear Viscosity of HMX. *Mech. Mater*. **2021**, *152*, 103644(1-12).

[18] Das, P.; Zhao, P.; Perera, D.; Sewell, T.; Udaykumar, H. S. Molecular Dynamics-Guided Material Model for the Simulation of Shock-Induced Pore Collapse in β-Octahydro-1,3,5,7-tetranitro-1,3,5,7-tetrazocine (β-HMX). *J. Appl. Phys*. **2021**, Submitted.

[19] Kroonblawd, M. P.; Mathew, N.; Jiang, S.; Sewell, T. D. A Generalized Crystal-Cutting Method for Modeling Arbitrarily Oriented Crystals in 3D Periodic Simulation Cells with Applications to Crystal-Crystal Interfaces. *Comput. Phys. Commun.* **2016**, *207*, 232-242.

[20] Baldridge, K. K.; Siegel, J. S. Balancing Steric and Electronic Factors in Push-Pull Benzenes: An Ab Initio Study on the Molecular Structure of 1,3,5-Triamino-2,4,6-Trinitrobenzene and Related Compounds. *J. Am. Chem. Soc.* **1993**, *115*, 10782-10785.

[21] Cady, H. H.; Larson, A. C. The Crystal Structure of 1,3,5-Triamino-2,4,6-Trinitrobenzene. *Acta Crystallogr.* **1965**, *18*, 485-496.

[22] Steele, B. A.; Clarke, S. M.; Kroonblawd, M. P.; Kuo, I.-F. W.; Pagoria, P. F.; Tkachev, S. N.; Smith, J. S.; Bastea, S.; Fried, L. E.; Zaug, J. M.; Stavrou, E.; Tschauner, O. Pressure-Induced Phase Transition in 1,3,5-Triamino-2,4,6-trinitrobenzene (TATB). *Appl. Phys. Lett.* **2019**, *114*, 191901(1-5).

[23] Bedrov, D.; Borodin, O.; Smith, G. D.; Sewell, T. D.; Dattelbaum, D. M.; Stevens, L. L. A Molecular Dynamics Simulation Study of Crystalline 1,3,5-Triamino-2,4,6-Trinitrobenzene as a Function of Pressure and Temperature. *J. Chem. Phys.* **2009**, *131*, 224703(1-13).

[24] Mathew, N.; Sewell, T. D. Generalized Stacking Fault Energies in the Basal Plane of Triclinic Molecular Crystal 1,3,5-Triamino-2,4,6-Trinitrobenzene (TATB). *Philos. Mag.* **2015**, *95*, 424-440.

[25] Lafourcade, P.; Denoual, C.; Maillet, J.-B. Dislocation Core Structure at Finite Temperature Inferred by Molecular Dynamics Simulations for 1,3,5-Triamino-2,4,6-Trinitrobenzene Single Crystal. *J. Phys. Chem. C* **2017**, *121*, 7442–7449.

[26] Mathew, N.; Sewell, T. D. Nanoindentation of the Triclinic Molecular Crystal 1.3.5-Triamino-2,4,6-Trinitrobenzene: A Molecular Dynamics Study. *J. Phys. Chem. C* **2016**, *120*, 8266-8277.

[27] Taw, M.R.; Yeager, J. D.; Hooks, D. E.; Carvajal, T. M.; Bahr, D. F. The Mechanical Properties of As-Grown Noncubic Organic Molecular Crystal Assessed by Nanoindentation. *J. Mater. Res.* **2017**, *32*, 2728-2737.

[28] Budzevich, M.; Conroy, M.; Landerville, A.; Lin, Y.; Oleynik, I.; White, C.T. Hydrostatic Equation of State and Anisotropic Constitutive Relationships in 1,3,5-Triamino-2,4,6-Trinitrobenzene (TATB). *AIP Conf. Proc.* **2010**, *1195*, 545-548.

[29] Lafourcade, P.; Denoual, C.; Maillet, J.-B. Irreversible Deformation Mechanisms for 1,3,5-Triamino-2,4,6-Trinitrobenzene Single Crystal through Molecular Dynamics Simulations. *J. Phys. Chem. C* **2018**, *122*, 14954-14964.

[30] Shimamura, K.; Misawa, M.; Ohmura, S.; Shimojo, F.; Kalia, R. K.; Nakano, A.; Vashishta, P. Crystalline Anisotropy of Shock-Induced Phenomena: Omni-Directional Multiscale Shock Technique. *Appl. Phys. Lett.* **2016**, *108*, 071901(1-5).

[31] Budzevich, M. M.; Landerville, A. C.; Conroy, M. W.; Lin, Y.; Oleynik, I. I.; White, C. T. Hydrostatic and Uniaxial Compression Studies of 1,3,5-Triamino-2,4,6-Trinitrobenzene Using Density Functional Theory with Van der Waals Correction. *J. Appl. Phys.* **2010**, *107*, 113524.

[32] Valenzano, L.; Slough, W. J.; Perger, W. F. Accurate Prediction of Second-Order Elastic Constants from Frist Principles: PETN and TATB. *AIP Conf. Proc.* **2012**, *1426*, 1191-1194.

[33] Zhang, C. Investigation of the Slide of the Single Layer of the 1,3,5-Triamino-2,4,6-Trinitrobenzene Crystal: Sliding Potential and Orientation. *J. Phys. Chem. B* **2007**, *111*, 14295-14298.

[34] Zhang, C.; Wang, X.; Huang, H. π-Stacked Interactions in Explosive Crystals: Buffers against External Mechanical Stimuli. *J. Am. Chem. Soc.* **2008**, *130*, 8359-8365.

[35] Kolb, J. R.; Rizzo, H. F. Growth of 1,3,5-Triamino-2,4,6-Trinitrobenzene (TATB). I. Anisotropic Thermal Expansion. *Propellants, Explos., Pyrotech.* **1979**, *4*, 10-16.

[36] Rizzo, H.F.; Kolb, J. R. Growth of 1,3,5-Triamino-2,4,6-Trinitrobenzene (TATB). II. Control of Growth by Use of High-Tg Polymeric Binders. *Propellants, Explos., Pyrotech.* **1981**, *6*, 57-62.

[37] Kroonblawd, M. P.; Sewell, T. D. Theoretical Determination of Anisotropic Thermal Conductivity for Crystalline 1,3,5-Triamino-2,4,6-Trinitrobenzene (TATB). *J. Chem. Phys.* **2013**, *139*, 074503(1-10).

[38] Kroonblawd, M. P.; Sewell, T. D. Theoretical Determination of Anisotropic Thermal Conductivity for Initially Defect-Free and Defective TATB Single Crystals. *J. Chem. Phys.* **2014**, *141*, 184501(1-10).

[39] Kroonblawd, M. P.; Sewell, T. D. Predicted Anisotropic Thermal Conductivity for Crystalline 1,3,5-Triamino-2,4,6-Trinitobenzene (TATB): Temperature and Pressure Dependence and Sensitivity to Intramolecular Force Field Terms. *Propellants, Explos., Pyrotech.* **2016**, *41*, 502-513.

[40] Mathew, N.; Sewell, T. D.; Thompson, D. L. Anisotropic in Surface-Initiated Melting of the Triclinic Molecular Crystal 1,3,5-Triamino-2,4,6-Trinitrobenzene: A Molecular Dynamics Study. *J. Chem. Phys*. **2015**, *143*, 094706(1-12).

[41] Gee, R. H.; Roszak, S.; Balasubramanian, K.; Fried, L. E. Ab Initio Based Force Field and Molecular Dynamics Simulations of Crystalline TATB. *J. Chem. Phys*. **2004**, *120*, 7059-7066.

[42] Fan, H.; Long, Y.; Ding, L.; Chen, J.; Nie, F.-D. A Theoretical Study of Elastic Anisotropy and Thermal Conductivity for TATB under Pressure. *Comput. Mater. Sci*. **2017**, *131*, 321-332.

[43] Long, Y.; Chen, J. Theoretical Study of the Phonon Spectrum, Phonon Refraction and Thermodynamic Properties for Explosive/Additive Interfaces. *Modelling Simul. Mater. Sci. Eng*. **2018**, *26*, 015002(1-20).

[44] Sun, J.; Kang, B.; Xue, C.; Liu, Y.; Xia, Y.; Liu, Y.; Zhang, W. Crystal State of 1,3,5-Triamino-2,4,6-Trinitrobenzene (TATB) Undergoing Thermal Cycling Process. *J. Energ. Mater*. **2010**, *28*, 189-201.

[45] Voigt-Martin, I. G.; Li, G.; Yakimanski, A. A.; Wolff, J. J.; Gross, H. Use of Electron Diffraction and High-Resolution Imaging to Explain Why the Non-Dipolar 1,3,5-Triamino-2,4,6-Trinitrobenzene Displays Strong Powder Second Harmonic Generation Efficiency. *J. Phys. Chem. A* **1997**, *101*, 7265-7276.

[46] Davidson, A. J.; Dias, R. P.; Dattelbaum, D. M.; Yoo, C. S. "Stubborn" Triaminotrinitrobenzene: Unusually High Chemical Stability of a Molecular Solid to 150 GPa. *J. Chem. Phys.* **2011**, *135*, 174507.

[47] Taylor, D. E. Intermolecular Forces and Molecular Dynamics Simulation of 1,3,5-Triamino-2,4,6-Trinitrobenzene (TATB) Using Symmetry Adapted Perturbation Theory. *J. Phys. Chem. A* **2013**, *117*, 3507-3520.

[48] LASL Explosive Property Data. Gibbs, T. R.; Popolato, A.; Baytos, J. F. (Eds.) (University of California Press, Berkeley, 1980).

[49] Fried, L. E.; Tarver, C. Molecular Dynamics Simulation of Shocks in Porous TATB Crystals. *AIP Conf. Proc.* **1996**, *370*, 179-184.

[50] Mayo, S. L.; Olafson, B. D.; Goddard III, W. A. DREIDING: A Generic Force Field for Molecular Simulations. *J. Phys. Chem.* **1990**, *94*, 8897-8909.

[51] Long, Y.; Chen, J. Theoretical Study of the Reaction Kinetics and the Detonation Wave Profile for 1,3,5-Triamino-2,4,6-Trinitrobenzene, *J. Appl. Phys.* **2016**, *120*, 185902(1-11).

[52] Zhang, L.; Zybin, S.V.; van Duin, A. C. T.; Dasgupta, S.; Goddard III, W. A.; Kober, E. M. Carbon Cluster Formation During Thermal Decomposition of Octahydro-1,3,5,7-Tetranitro-1,3,5,7-Tetrazocine and 1,3,5-Triamino-2,4,6-Trinitrobenzene High Explosives from ReaxFF Reactive Molecular Dynamics Simulations. *J. Phys. Chem. A* **2009**, *113*, 10619-10640.

[53] Liu, L.; Liu, Y.; Zybin, S. V.; Sun, H.; Goddard III, W. A. ReaxFF-*l*g: Correction of the ReaxFF Reactive Force Field for London Dispersion, with Applications to the Equations of State for Energetic Materials. *J. Phys. Chem. A* **2011**, *115*, 11016-11022.

[54] Traver, C. M. Ignition and Growth Modeling of LX-17 Hockey Puck Experiment. *Propellants, Explos. Pyrotech*. **2005**, *30*, 109-117.

[55] Long, Y.; Chen, J. An Investigation of the Hot Spot Formation Mechanism for Energetic Material. *J. Appl. Phys*. **2017**, *122*, 175105(1-10).

[56] Kroonblawd, M. P.; Fried, L. E. High Explosive Ignition through Chemically Activated Nanoscale Shear Bands. *Phys. Rev. Lett*. **2020**, *124*, 206002(1-6).

[57] Hamilton, B. W.; Kroonblawd, M. P.; Li, C.; Strachan, A. A Hotspot's Better Half: Non-Equilibrium Intra-Molecular Strain in Shock Physics. *J. Phys. Chem. Lett*. **2021**, *12*, 2756-2762.

[58] Reed, E. J.; Fried, L. E.; Joannopoulos, J. D. A Method for Tractable Dynamical Studies of Single and Double Shock Compression. *Phys. Rev. Lett*. **2003**, *90*, 235503(1-4).

[59] Tiwari, S. C.; Nomura, K.; Kalia, R. K.; Nakano, A.; Vashishta, P. Multiple Reaction Pathways in Shocked 2,4,6-Triamino-1,3,5-trinitrobenzene Crystal. *J. Phys. Chem. C*. **2017**, *121*, 16029-16034.

[60] Tarver, C. M.; Kury, J. W.; Breithaupt, R. D. Detonation Waves in Triaminotrinitrobenzene. *J. Appl. Phys*. **1997**, *82*, 3771-3782.

[61] Manaa, M. R.; Reed, E. J.; Fried, L. E.; Goldman, N. Nitrogen-Rich Heterocycles as Reactivity Retardants in Shocked Insensitive Explosives. *J. Am. Chem. Soc*. **2009**, *131*, 5483-5487.

[62] He, Z.; Chen, J.; Wu, Q. Initial Decomposition of Condensed-Phase 1,3,5-Triamino-2,4,6-trinitrobenzene under Shock Loading. *J. Phys. Chem. C*. **2017**, *121*, 8227-8235.

[63] Qi, T.; Reed, E. J. Simulations of Shocked Methane Including Self-Consistent Semiclassical Quantum Nuclear Effects. *J. Phys. Chem. A*. **2012**, *116*, 10451-10459.

[64] Hamilton, B. W.; Kroonblawd, M. P. Islam, M. M.; Strachan, A. Sensitivity of the Shock Initiation Threshold of 1,3,5-Triamino-2,4,6-trinitrobenzene (TATB) to Nuclear Quantum Effects. *J. Phys. Chem. C*. **2019**, *123*, 21969-21981.

[65] Kroonblawd, M. P.; Sewell, T. D.; Maillet, J.-B. Characteristics of Energy Exchange Between Inter- and Intramolecular Degrees of Freedom in Crystalline 1,3,5-Triamino-2,4,6-Trinitrobenzene (TATB) with Implications for Coarse-Grained Simulations of Shock Waves in Polyatomic Molecular Crystals. *J. Chem. Phys.* **2016**, *144*, 064501(1-14).

[66] Strachan, A.; Holian, B. L. Energy Exchange between Mesoparticles and Their Internal Degrees of Freedom. *Phys. Rev. Lett*. **2005**, *94*, 014301(1-4).

[67] Manna, R.; Fried, L. E. Nearly Equivalent Intra- and Intermolecular Hydrogen Bonding in 1,3,5-Triamino-2,4,6-Trinitrobenzene at High Pressure. *J. Phys. Chem. C* **2011**, *116*, 2116-2122.

[68] Ojeda, O.U.; Çağın, T. Hydrogen Bonding and Molecular Rearrangement in 1,3,5-Triamino-2,4,6-Trinitrobenzene under Compression. *J. Phys. Chem. B* **2011**, *115*, 12085-12093.

[69] Steele, B. A.; Stavrou, E.; Prakapenka, V. B.; Kroonblawd, M. P.; Kuo, I.-F. W. High-Pressure Equation of State of 1,3,5-Triamino-2,4,6-Trinitrobenzene: Insights into the Monoclinic Phase Transition, Hydrogen Bonding, and Anharmonicity. *J. Phys. Chem. A*. **2020**, *124*, 10580-10591.

[70] Delavignette P. Dissociation and Plasticity of Layered Crystals. *Le J. Phys. Colloq.* **1974**, *35*, 181-187.

[71] Pineau, N. Molecular Dynamics Simulations of Shock Compressed Graphite. *J. Phys. Chem. C* **2013**, *117*, 12778-12786.

[72] Onsager, L. Electric Moments of Molecules in Liquids. *J. Am. Chem. Soc*. **1936**, *58*, 1486-1493.

[73] Barker, J. A.; Watts, R. O. Monte Carlo Studies of the Dielectric Properties of Water-Like Models. *Mol. Phys.* **1973**, *26*, 789-792.

[74] Watts, R. O. Monte Carlo Studies of Liquid Water. *Mol. Phys*. **1974**, *28*, 1069-1083.

[75] Travis, J. R. "TATB: The IHE Exemplar," Report No. LA-UR-92-3883, 1992.

[76] Dobratz, B. M. "The Insensitive High Explosive Triaminotrinitrobenzene "TATB": Development and Characterization—1888 to 1994," Report No. LA-13014-H, 1995.

[77] Hoffman, D. M.; Willey, T. M.; Mitchell, A. R.; Depiero, S. C. Comparison of New and Legacy TATBs. *J. Energ. Mater.* **2008**, *26*, 139-162.

[78] Plimpton, S. Fast Parallel Algorithms for Short-Range Molecular Dynamics. *J. Comp. Phys.* **1996**, *117*, 1-19.

[79] LAMMPS is available at http://lammps.sandia.gov.

[80] Kroonblawd, M. P.; Sewell, T. D. Anisotropic Relaxation of Idealized Hot Spots in Crystalline 1,3,5-Triamino-2,4,6-Trinitrobenzene (TATB). *J. Phys. Chem.* **2016**, *120*, 17214-17223.

[81] Mathew, N.; Kroonblawd, M. P.; Sewell, T. D.; Thompson, D. L. Predicted Melt Curve and Liquid-State Transport Properties of TATB from Molecular Dynamics Simulations. *Mol. Simul.* **2018**, *44*, 613-622.

[82] Holian, B. L.; Lomdahl, P. S. Plasticity Induced by Shock Waves in Nonequilibrium Molecular-Dynamics Simulations. *Science* **1998**, *280*, 2085-2088.

[83] Zel'dovich, Y. B.; Raizer, Y. P. Physics of Shock Waves and High-Temperature Hydrodynamic Phenomena (Dover, Mineola, NY, 2002) Editors: Hayes, W. D.; Probstein, R. F.

[84] Verlet, L. Computer "Experiments" on Classical Fluids. I. Thermodynamical Properties of Lennard-Jones Molecules. *Phys. Rev.* **1967**, *159*, 98-103.

[85] Nosé, S. A Unified Formulation of the Constant-Temperature Molecular-Dynamics Methods. *J. Chem. Phys.* **1984**, *81*, 511-519.

[86] Hoover, W. G. Canonical Dynamics: Equilibrium Phase-Space Distributions. *Phys. Rev. A* **1985**, *31*, 1695-1697.

[87] Siavosh-Haghighi, A.; Dawes, R.; Sewell, T. D.; Thompson, D. L. Shock-Induced Melting of (100)-Oriented Nitromethane: Structural Relaxation. *J. Chem. Phys.* **2009**, *131*, 064503(1-9).

[88] He, L.; Sewell, T. D.; Thompson, D. L. Molecular Dynamics Simulations of Shock Waves in Oriented Nitromethane Single Crystals. *J. Chem. Phys.* **2011**, *134*, 124506(1-12).

[89] Eason, R. M.; Sewell, T. D. Shock-Induced Inelastic Deformation in Oriented Crystalline Pentaerythritol Tetranitrate. *J. Phys. Chem. C*. **2011**, *116*, 2226-2239.

[90] Zimmerman, J. A.; Kelchner, C. L.; Klein, P. A.; Hamilton, J. C.; Foiles, S. M. Surface Step Effects on Nanoindentation. *Phys. Rev. Lett*. **2001**, *87*, 165507(1-4).

[91] Jaramillo, E.; Sewell, T. D.; Strachan, A. Atomic-Level View of Inelastic Deformation in a Shock Loaded Molecular Crystal. *Phys. Rev. B* **2007**, *76*, 064112(1-6).

[92] Petit, A.-T.; Dulong, P.-L. Recherches sur Quelques Points Importants de la Théorie de la Chaleur. *Annales de Chimie et de Physique (in French)*. **1819**, *10*, 395-413.

[93] Cawkwell, M. J.; Sewell, T. D.; Zheng, K.; Thompson, D. L. Shock-Induced Shear Bands in an Energetic Molecular Crystal: Application of Shock-Front Absorbing Boundary Conditions to Molecular Dynamics Simulations. *Phys. Rev. B* **2008**, *78*, 014107(1-13).

[94] Fröhlich, M. G.; Sewell, T. D.; Thompson, D. L. Molecular Dynamics Simulations of Shock Waves in Hydroxyl-Terminated Polybutadiene Melts: Mechanical and Structural Responses. *J. Chem. Phys.* **2014**, *140*, 024902(1-12).

[95] Bringa, E. M.; Caro, A.; Wang, Y.; Victoria, M.; McNaney, J. M.; Remington, B. A.; Smith, R. F.; Torralva, B. R.; Swygenhove, H. V. Ultrahigh Strength in Nanocrystalline Materials under Shock Loading. *Science*, **2005**, *209*, 1838-1841.

[96] Crowhurst, J. C.; Armstrong, M. R.; Knight, K. B.; Zaug, J. M.; Behymer, E. M. Invariance of the Dissipative Action at Ultrahigh Strain Rates above the Strong Shock Threshold. *Phys. Rev. Lett.* **2011**, *107*, 144302(1-5).

[97] Rivera-Rivera, L. A.; Sewell, T. D.; Thompson, D. L. Post-Shock Relaxation in Crystalline Nitromethane. *J. Chem. Phys*. **2013**, *138*, 084512(1-8).

[98] Dawes, R.; Siavosh-Haghighi, A.; Sewell, T. D.; Thompson, D. L. Shock-Induced Melting of (100)-Oriented Nitromethane: Energy Partitioning and Vibrational Mode Heating. *J. Chem. Phys*. **2009**, *131*, 224513(1-11).

[99] Jiang, S.; Sewell, T. D.; Thompson, D. L. Molecular Dynamics Simulations of Shock Wave Propagation through the Crystal-Melt Interface of (100)-Oriented Nitromethane. *J. Phys. Chem. C*. **2016**, *120*, 22989-23000.
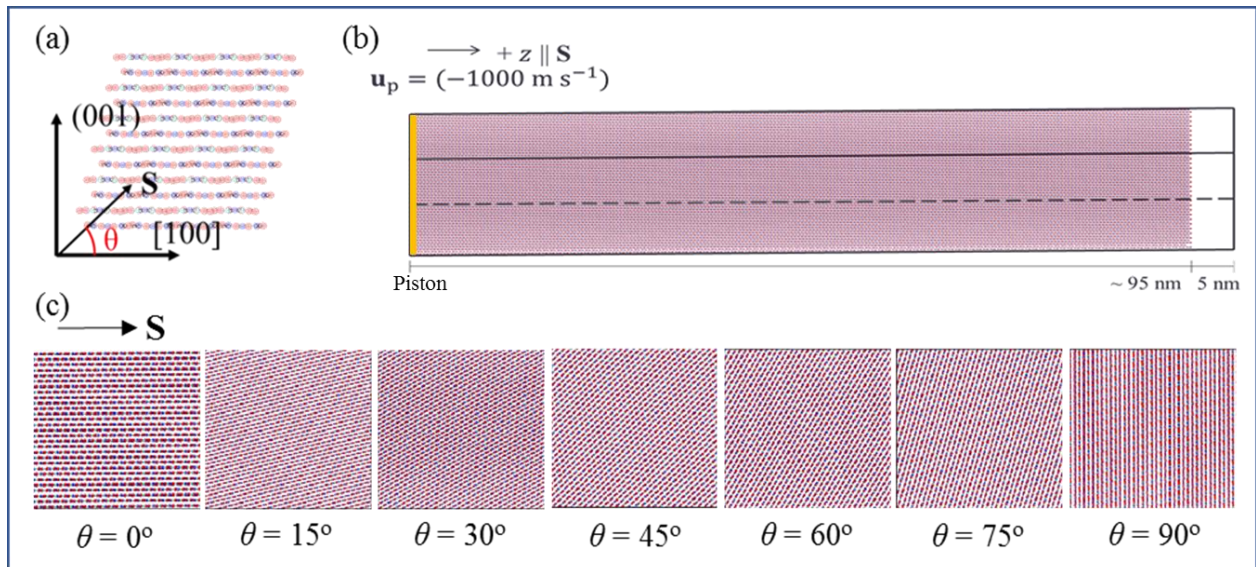
Figure 1. Definitions of the (a) orientation angle θ and (b) simulation set-up. (c) 2D projections of the simulation cells along the shock direction for all seven orientations. For $\theta = 0°$ and 90°, the shock propagation direction **S** is exactly parallel and exactly perpendicular, respectively, to the graphitic-like molecular layers in the crystal.
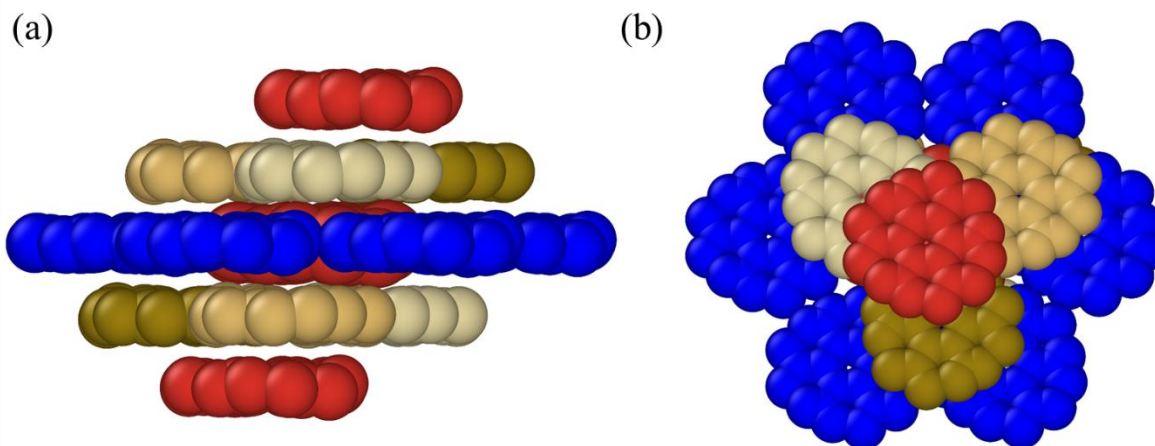
Figure 2. Depiction of a central molecule (red, large atoms) along with six in-plane near neighbors (navy) and eight out-of-plane near neighbors (shades of brown and red). (a) Side view; (b) Top view. The red molecules two layers above and below the central molecule are symmetry equivalents to the central one. An analogous coloring scheme—navy for in-plane neighbors and brown for out-of-plane ones—is used in **Figure 10**.
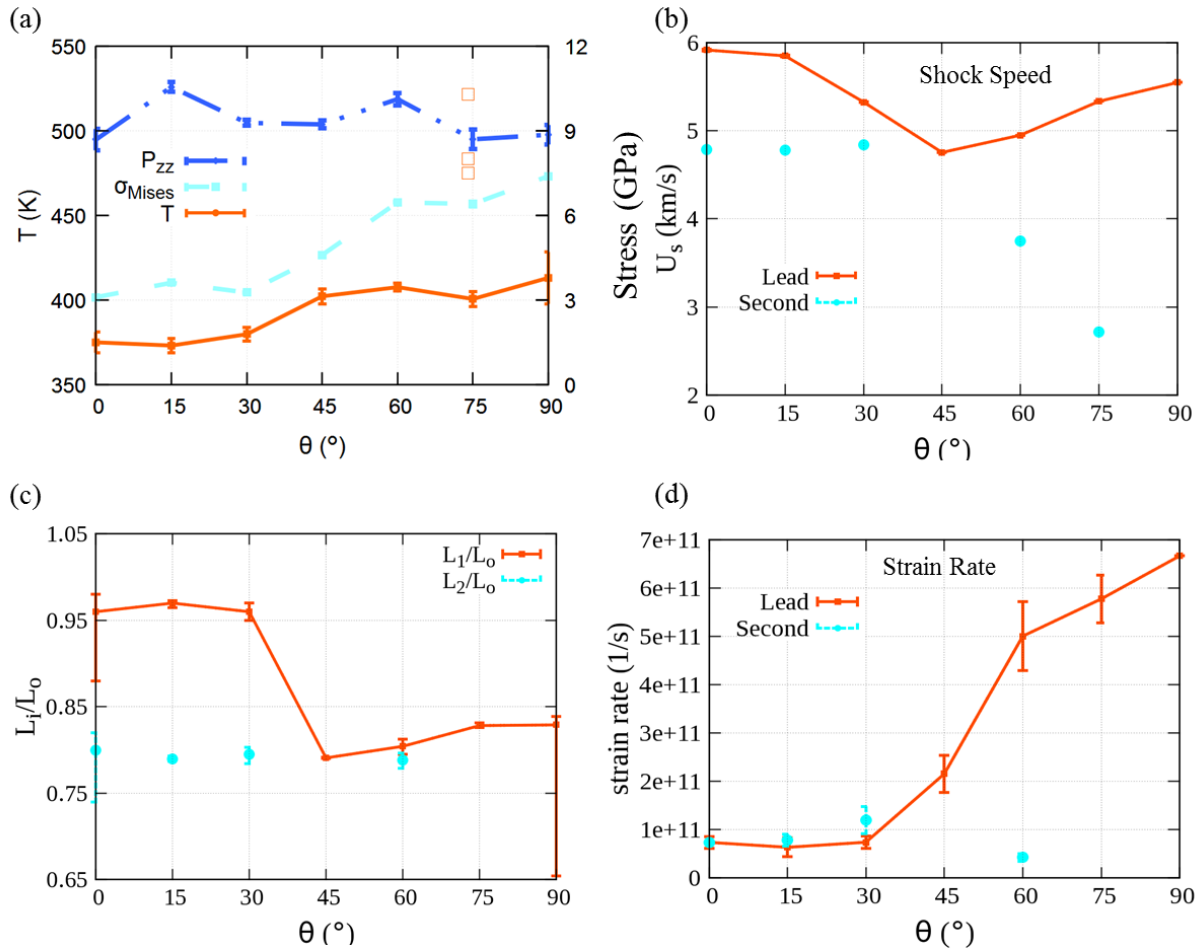
Figure 3. Orientation-dependent thermal and mechanical properties. (a) Kinetic temperature T (red, left-hand ordinate), threshold von Mises stress σ_{Mises} (blue, right-hand ordinate), and longitudinal stress component P_{zz} (navy, right-hand ordinate) evaluated well behind the final shock. (b) Propagation speeds for the lead (red) and second (blue) shocks. (c) Compression ratios calculated behind the lead shock (L_1/L_0, red) and behind the second shock (L_2/L_0, blue). (d) Strain rates during shock rises for the lead shock (red) and second shock (blue).
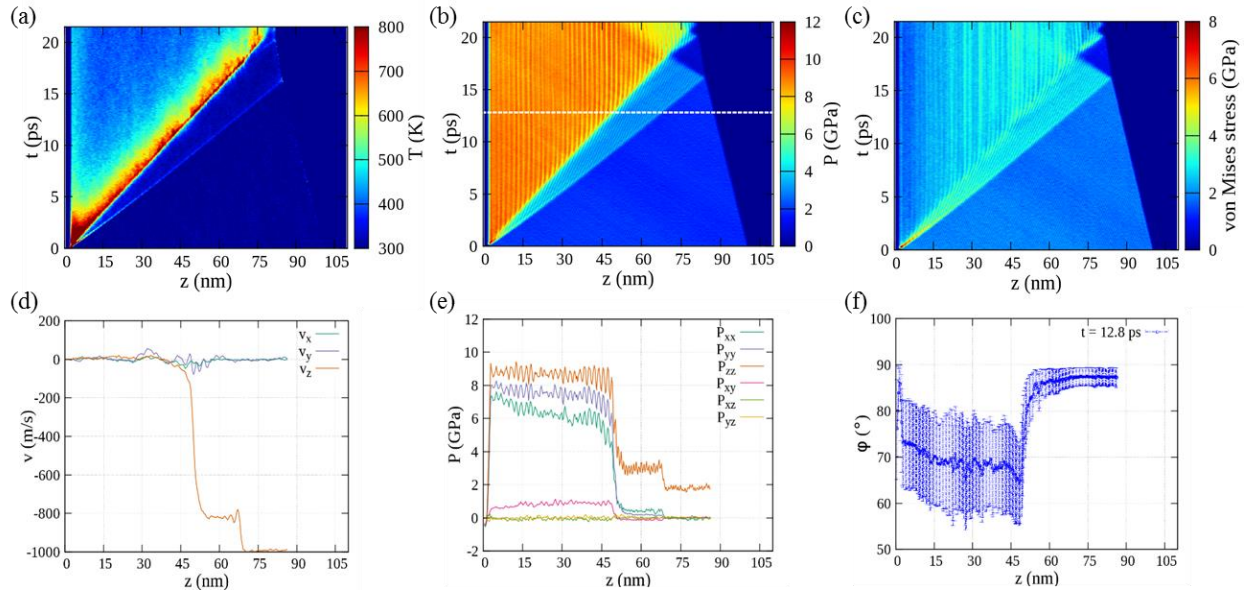
Figure 4. Top row: Time-position (*t-z*) diagrams for shock orientation angle $\theta = 0°$. Intermolecular kinetic energy, (b) longitudinal stress component P_{zz}, (c) von Mises stress. Bottom row: Profiles across the length of the simulation cell for: (d) particle velocity components, (e) stress tensor components, (f) molecular orientation parameter. The instant of analysis in panels (d)-(f) is indicated by the white dashed horizontal line in panel (b).
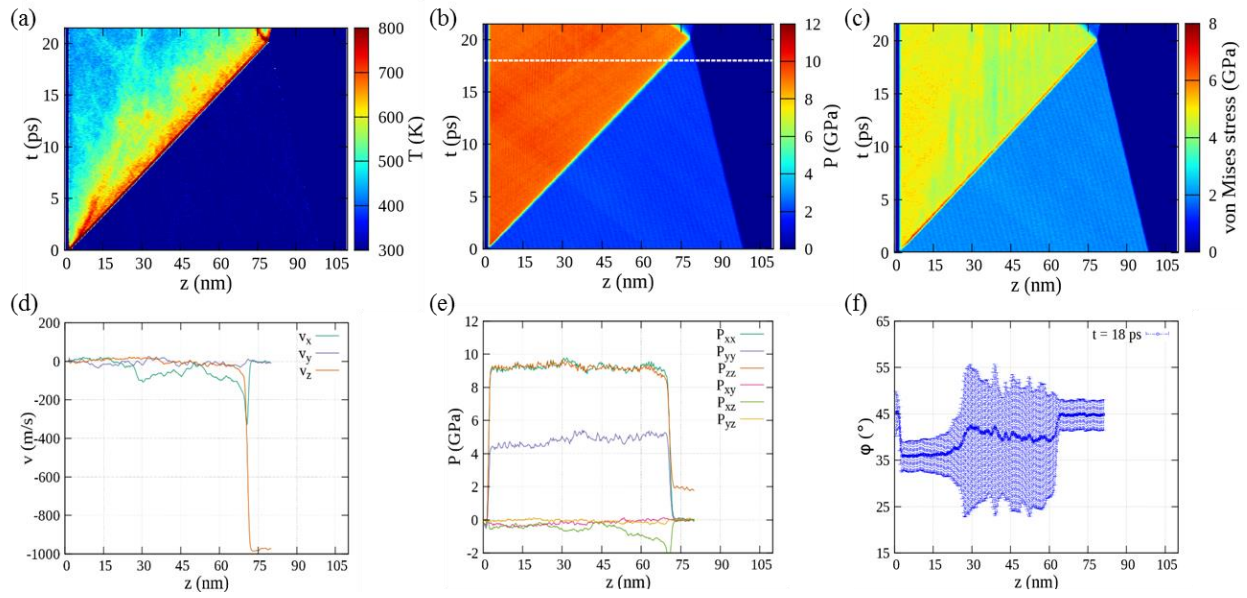
Figure 5. As in **Figure 4** but for shock orientation angle $\theta = 45°$.
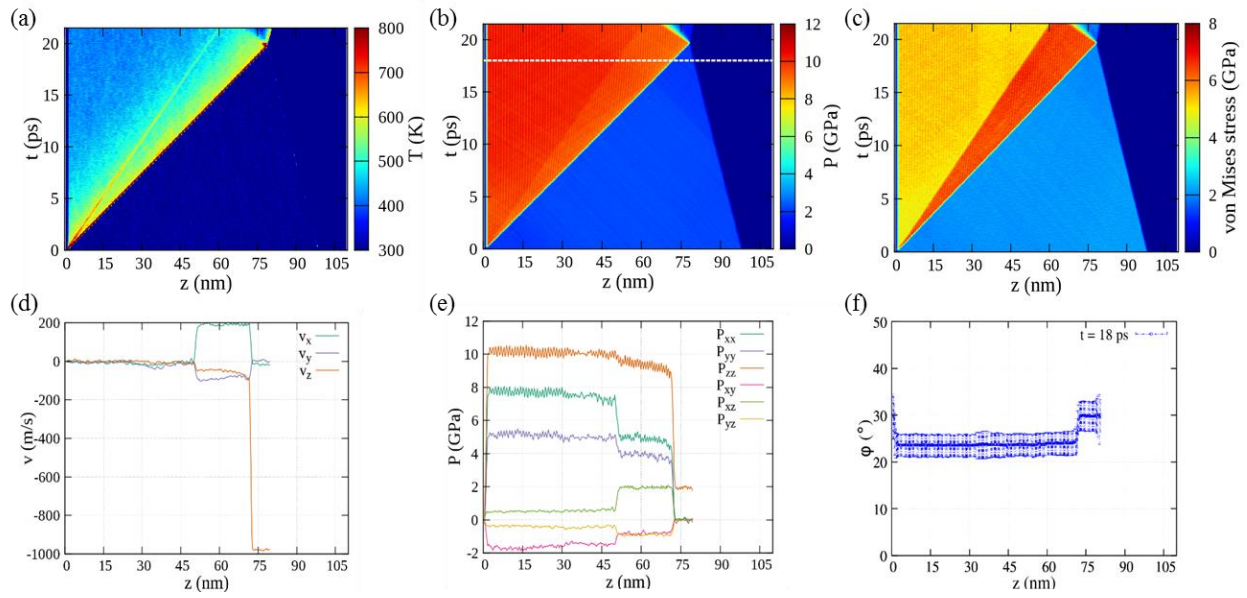
Figure 6. As in **Figures 4-5** but for shock orientation angle $\theta = 60°$.
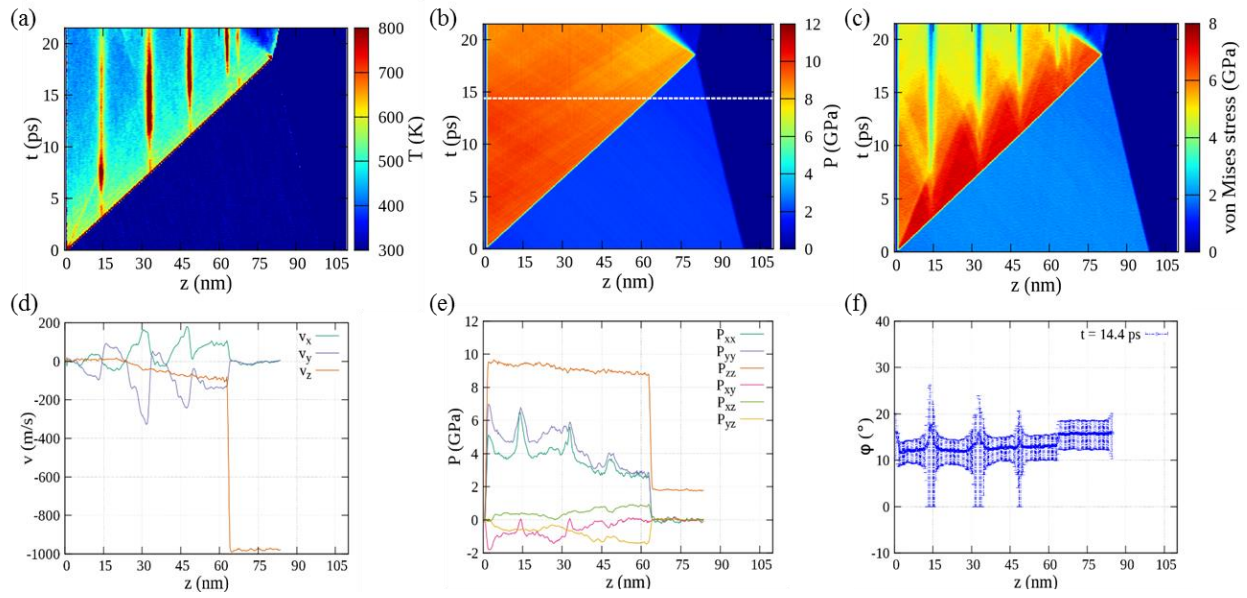
Figure 7. As in **Figures 4-6** but for shock orientation angle $\theta = 75°$.
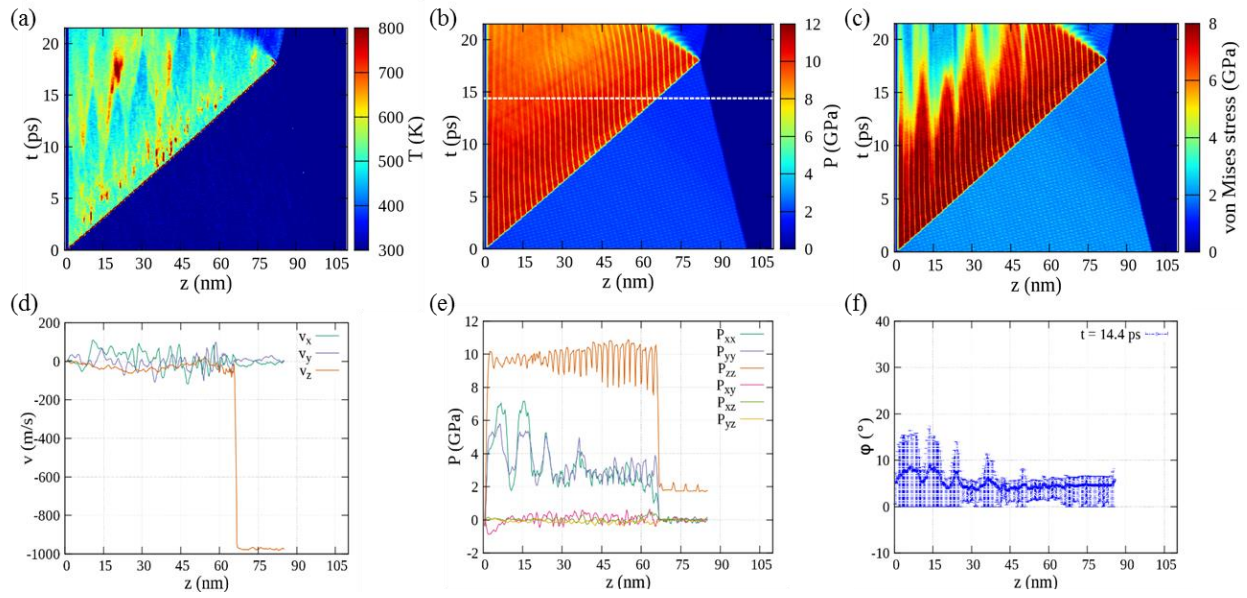
**Figure 8.** As in **Figures 4-7** but for shock orientation angle $\theta = 90°$.
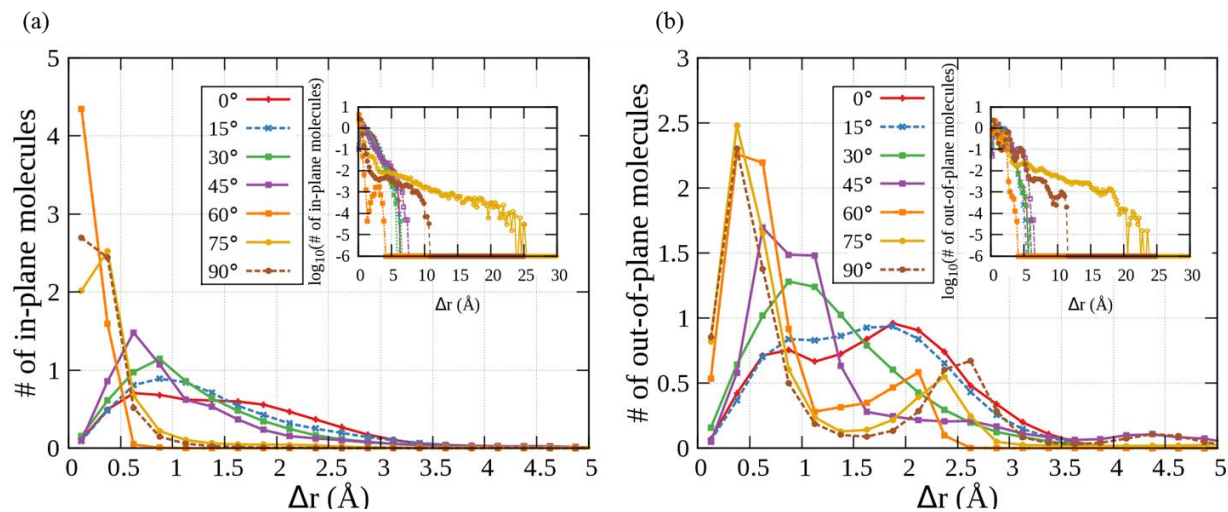
Figure 9. Distribution functions for NNRDs for (a) the six in-plane and (b) eight out-of-plane near-neighbor molecules for all seven orientations. The insets show the same results on a $\log_{10}$-linear scale.
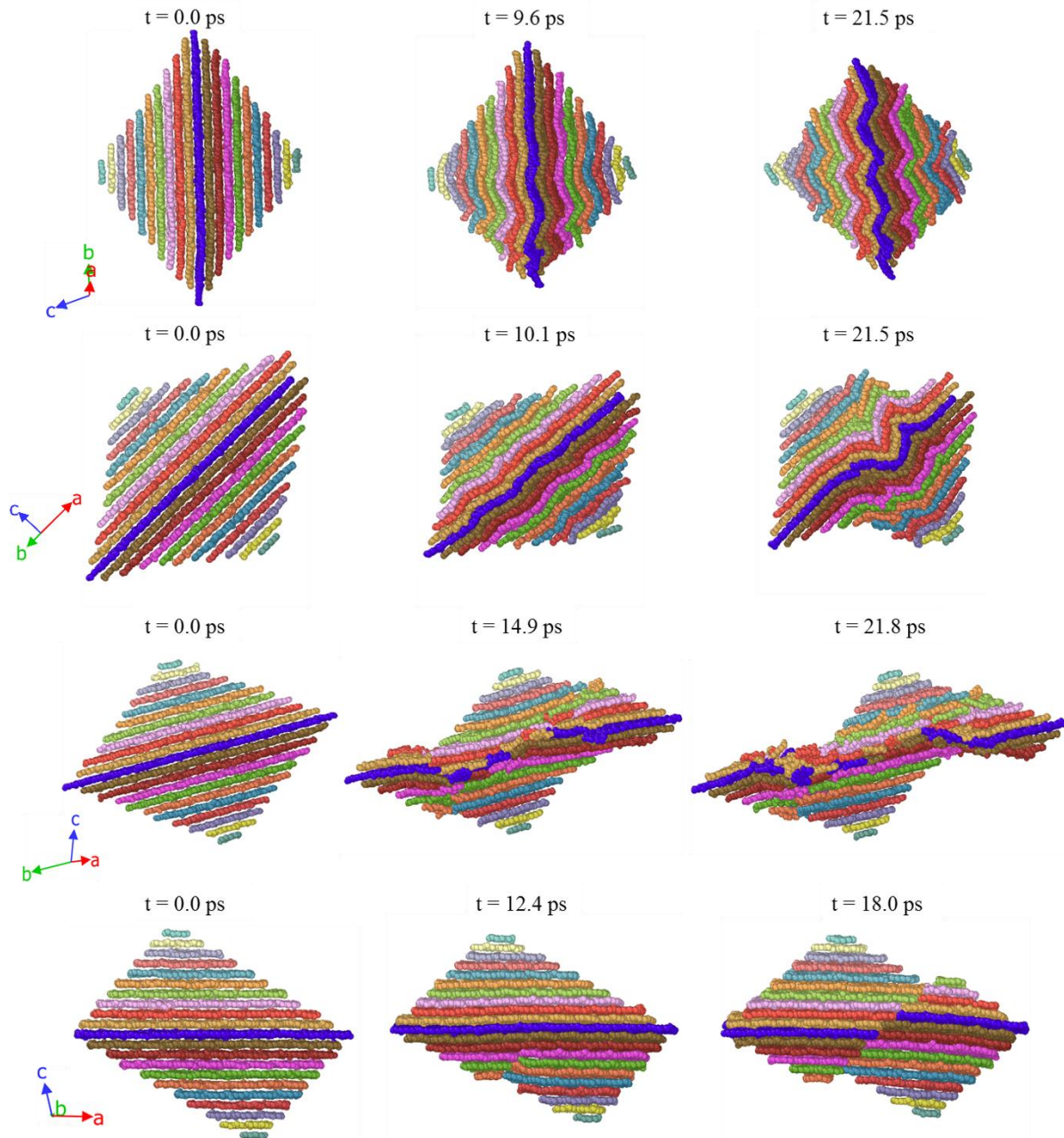
Figure 10. From top to bottom, snapshots at a time t of a selected molecule and its 670 closest neighbor molecules are shown for $\theta = 0°$, 45°, 75° and 90°. Molecular layers are colored according to distances away from the selected molecule. The central layer is in navy, immediately adjacent layers are shown in shades of brown, next-adjacent layers are in shades of red, and so on. The crystal lattice frames are shown on the left.
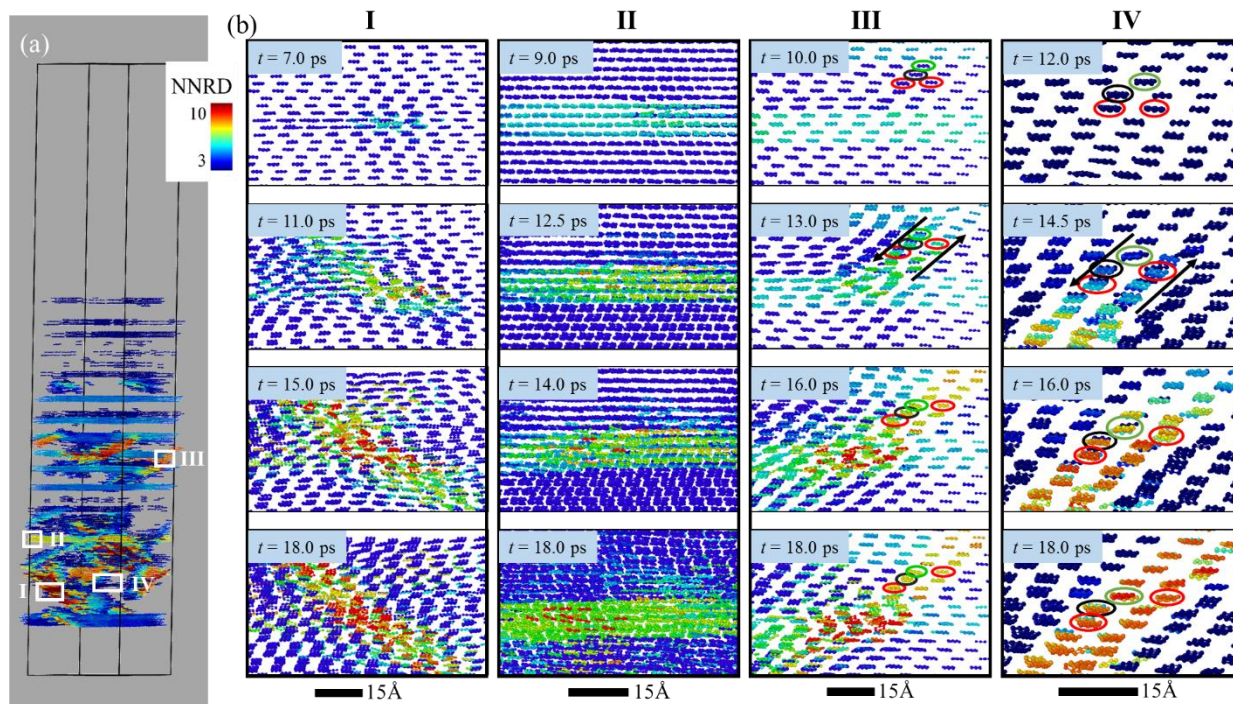
Figure 11. Deformation mechanisms for $\theta = 90°$. (a) A simulation snapshot, colored by NNRDs, for the system at the instant of maximum compression. (b) Zoom-in views of four selected regions (I-IV) showing a variety of deformation mechanisms. The four regions are indicated in panel (a).
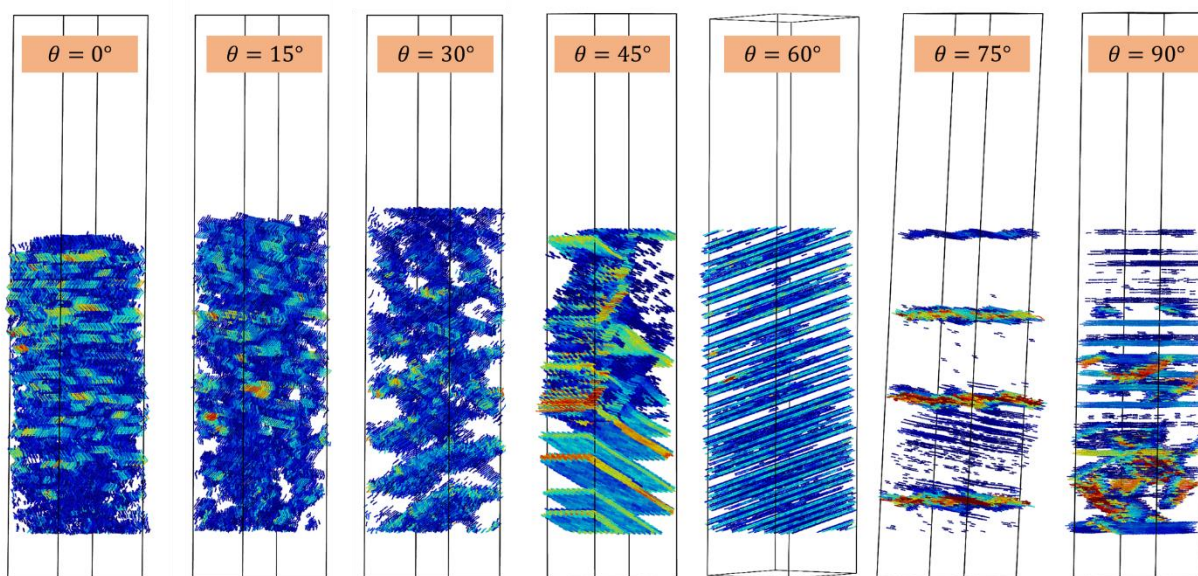
Figure 12. Simulation cell snapshots at the instants of maximum compression for (left-to-right) $\theta = 0°$, 15º, 30º, 45º, 60º, 75º, and 90º. Only molecules for which the maximum displacement between it and any of its 14 neighbor molecules exceeds a threshold value (varies with orientation) are shown, and these are colored according to the value of that displacement.

TABLE OF CONTENT